January 2016

CHARACTERIZATION OF HETEROGENEOUS CATALYSTS USING ADVANCED TRANSMISSION ELECTRON MICROSCOPY TECHNIQUES

Chang Wan Han
Purdue University

Graduate School Form
30 Updated 12/26/2015

PURDUE UNIVERSITY
GRADUATE SCHOOL
Thesis/Dissertation Acceptance

This is to certify that the thesis/dissertation prepared

By Chang Wan Han

Entitled

CHARACTERIZATION OF HETEROGENEOUS CATALYSTS USING ADVANCED TRANSMISSION ELECTRON MICROSCOPY TECHNIQUES

For the degree of Doctor of Philosophy

Is approved by the final examining committee:

Volkan Ortalan
Chair

Eric P. Kvam

Lia A. Stanciu

Alejandro H. Strachan

To the best of my knowledge and as understood by the student in the Thesis/Dissertation Agreement, Publication Delay, and Certification Disclaimer (Graduate School Form 32), this thesis/dissertation adheres to the provisions of Purdue University's "Policy of Integrity in Research" and the use of copyright material.

Approved by Major Professor(s): Volkan Ortalan

Approved by: David F. Bahr 11/17/2016

Head of the Departmental Graduate Program Date

CHARACTERIZATION OF HETEROGENEOUS CATALYSTS USING ADVANCED TRANSMISSION ELECTRON MICROSCOPY TECHNIQUES

A Dissertation

Submitted to the Faculty

of

Purdue University

by

Chang Wan Han

In Partial Fulfillment of the

Requirements for the Degree

of

Doctor of Philosophy

December 2016

Purdue University

West Lafayette, Indiana

For my parents

ACKNOWLEDGEMENTS

This dissertation would not be completed without the support from many people. First of all, I would like to thank my major advisor, Prof. Volkan Ortalan for assigning the transmission electron microscopy research project, which I really enjoy as much as I want to keep work on for the entire my life. Through this project, I could learn advanced microscopy techniques, met good collaborators, and had a chance to operate several state-of-the-art microscopes. I appreciate him for these chances as well as for his guidance.

I thank Profs. Eric Kvam, Alejandro Strachan, and Lia Stanciu for serving my dissertation committee and for spending a significant of their time for reviewing my dissertation. They also taught me a lot in and outside of class: Prof. Kvam is the person who was the instructor of four courses - Microstructural characterization techniques, TEM skills, Defects in solids, Phase transformation and I really enjoyed his classes. Especially, his microstructural characterization class and TEM class were highly useful for my entire Ph.D. studies. Prof. Strachan is the professor whom I like in terms of his mentorship as well as his research. I remembered that he reviewed my first quantum mechanics homework together and kindly gave comments. Although his two courses on atomistic simulations of materials were the most difficult courses for me, those courses opened possibilities for me to utilize theoretical simulations in my research.

Prof. Stanciu is the person who most frequently publishes research papers in our department. Every time I get an update on her new publications, I am always motivated.

I thank Prof. Fabio Ribeiro and his students, Dr. Yanran Cui and Corry Milligan contributed to my Au-Fe_3O_4 projects by measuring catalytic activities and by performing *in-situ* XPS. I also thank Prof. Jeffrey Greeley and his students, Paulami Majumdar and Tej Choski for their contributions to my AuIr-TiO_2 and Au-Fe_3O_4 papers by performing theoretical Density Functional Theory calculations, which was useful to understand the metal-support interactions within my material system. Prof. Chao Wang and his student Michael Manto should also be acknowledged for their contributions on my work by providing many interesting samples, such as the heterodimer dumbbell-like nanoparticles.

I appreciate Dr. Singanallur Venkatakrishnan for providing a great tomography reconstruction code and helping me several times to troubleshoot problems during the tomography reconstruction. Dr. Raymond Unocic and Dr. Xiahan Sang at Oak Ridge National Laboratory are highly acknowledged in that they arranged multiple microscopy sessions and supported me to collect *in-situ* TEM data.

I would like to thank Dr. Sergey Suslov and Dr. Cem Akatay who provided me initial trainings for the Purdue FEI Titan E-TEM. I also thank Dr. Alan Nicholls at University of Illinois at Chicago who taught me how to operate a probe-corrected JEOL ARM200CF. I am also thankful to Prof. Patrick Cantwell of Rose Hulman Institute of Technology, who kindly replied back to my numerous questions on micro XRD measurements and texture quantifications using a MAUD Rietveld refinement software. Thanks to his help, I could manage my first project, which was a part of NNSA PRISM

project. I thank Ken Hibler, a field service engineer of FEI company in that he helped me to troubleshoot frequent instrumental issues of the microscopes on Purdue campus.

My undergraduate, master advisor Prof. Sang Ho Lim of Korea University is also highly appreciated. He is the person, who made me realize the enjoyment of doing materials science research. If I had not met him, I would not pursue a research scientist career.

Lastly, I am sincerely grateful to my family: My brother, who also got his Ph.D. at Purdue University motivates me in every aspect. Moreover, he and my sister-in-law helped me from A to Z of my new life until they moved to Nashville, TN. I would have a lot of trouble without their help. I am wholeheartedly grateful to my parents who always pray for me, encourage me, and be supportive of me during my entire life. Their unconditional love and support will never be forgotten.

My PhD studies were made possible by the financial support of the National Science Foundation Designing Materials to Revolutionize and Engineering our Future (DMRFE) initiative Design of next-generation catalysts through predictive modeling and atomic-scale experiments under Award Number CBET-1437219, the Department of Energy NNSA Center for Prediction of Reliability, Integrity, and Survivability of Microsystems under Award Number DE-FC52-08NA28617, the startup funding of the Purdue School of Materials Engineering, and an assistantship provided by Purdue Birck Nanotechnology Center.

TABLE OF CONTENTS

Page

LIST OF FIGURES

Figure Page

Figure Page

Figure Page

Figure Page

ABSTRACT

Chang Wan Han, Ph. D., Purdue University, December 2016. Characterization of Heterogeneous Catalysts using Advanced Transmission Electron Microscopy Techniques. Major Professor: Volkan Ortalan.

A heterogeneous catalyst is one of the most indispensable materials in industry and our daily life. Approximately 85-90% of the chemical products are made by utilizing catalytic processes. Moreover, heterogeneous catalysts are heavily used to clean up the exhaust gases and to prevent pollutions. In this regard, developing a novel heterogeneous catalyst having a long lifetime as well as an excellent catalytic activity, selectivity is crucial to sustain our modern society. Since this requires a clear understanding on the correlations between catalytic properties and structures of the catalyst, characterization of catalysts is an essential part of the heterogeneous catalysts research. However, this can often be a daunting challenge, because the structural components determining the catalytic properties have many different length scales from atomic to macro-scale. Furthermore, the microstructures of the catalysts are dynamically changed as the catalysts are exposed to reactive environments, such as gaseous and liquid reactants, heat, and etc.

The focus of this dissertation is to develop and apply advanced transmission electron microscopy (TEM) techniques, such as electron tomography (ET), aberration-corrected scanning TEM (AC-STEM), and *in-situ* TEM to solve challenging problems in the field of heterogeneous catalysis.

Major questions being addressed in this dissertation are closely related to the sintering phenomena, including the "surface migration mechanism" of catalytic nanoclusters, the correlations between "three dimensional (3D) structures of catalysts and thermal stability," and "thermal behaviors" of catalytic nanoparticles at high temperatures. Specifically, fast-scan high angle annular dark-field (HAADF) AC-STEM probed the surface migration behavior, which is one of the most fundamental steps of the sintering process (especially, Ostwald ripening), of Ir atoms and clusters on MgO surfaces at ~ 100 msec temporal resolution. Moreover, 3D structural information of ZnO mesotripod and AuIr bimetallic catalysts was obtained using ET and quantitatively analyzed 3D structure was correlated with the thermal stability. Finally, *in-situ* TEM visualized the real-time morphological changes and the thermal behaviors of Au-Fe_3O_4 dumbbell nanoparticle catalysts at high temperatures.

CHAPTER 1. INTRODUCTION

Catalysts are indispensable in modern chemical industries. Most chemical products (approximately, 85-90%) are made through catalytic processes.[1] Moreover, catalysts have been used to clean up exhaust gases from chemical plants and automobiles. In this regard, catalysts can be considered as one of the most important engineered materials in our modern society.

Modern catalysts are traditionally categorized as *homogeneous*, *heterogeneous*, and *bio catalysts*; homogeneous catalysts have the same phase with the reactant substances. That is, in homogeneous catalysis, catalysts will be liquid (or gas), if reactants are in liquid (or gaseous) phase. Bio catalysts are a sort of proteins having enzymatic functions. Heterogeneous catalysts have a different phase (mostly, solids) with reactants having a form of liquid or gaseous phase. Therefore, heterogeneous catalysts have been preferred in chemical industries in that they can be easily separated from reactants and products. Most of heterogeneous catalysts are solid phases being comprised of nanoparticles dispersed on a high surface area support as shown in Figure 1.1.

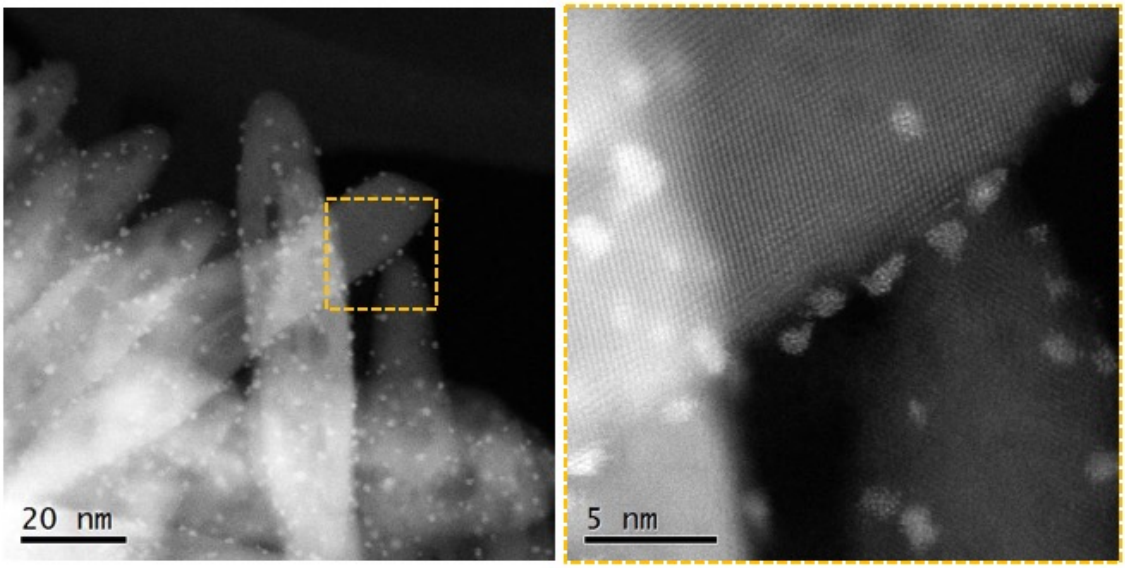

Figure 1.1 Z-contrast scanning transmission electron microscopy images of gold nanoparticles supported on titania (rutile) support. Due to the nature of Z-contrast imaging, gold nanoparticles (Z=79) show higher intensities with compared to titania support. Due to the nature of Z-contrast imaging, gold nanoparticles (Z=79) show higher intensities with compared to titania support (effective Z=12.7).

In this regard, developing a novel heterogeneous catalyst having a long lifetime with a superior catalytic activity/selectivity is crucial to sustain our society. Since this requires a clear understanding on the correlations between the catalytic properties and structures of the catalysts, a characterization of catalysts is an essential part of the heterogeneous catalyst research.

However, this can often be a daunting challenge. Since the structural components determining the catalytic properties have many different length scales from atomic to macro-scale as shown in Figure 1.2.[1]: Fundamental catalytic reaction, such as a bond breakage of reactant and a bond formation of product occur at a molecular level. In these fundamental steps, the atomic scale catalytic active sites (low coordinate atoms at corners and perimeters of nanoparticles[2]) play a significant role. Transport phenomena, such as the diffusion of reactant molecules through the pores of support materials also affects the rate of heterogeneous catalysis. Therefore, nano and/or macroscale pore distributions might also be considered for a clear understanding.

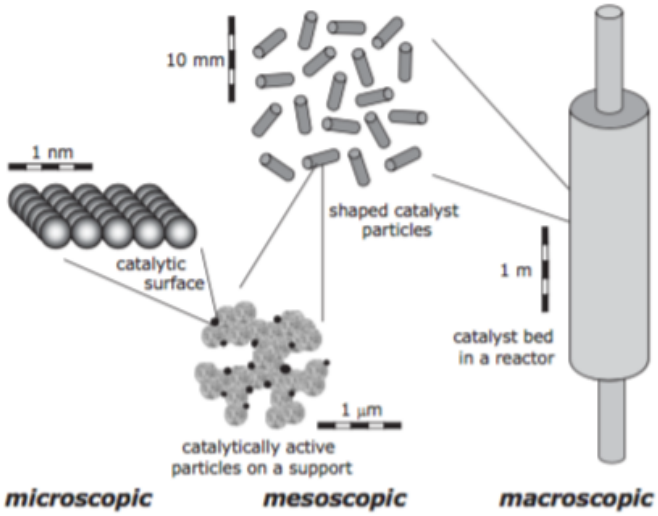

Figure 1.2 A schematic showing a large length scales in heterogeneous catalysis (Image adapted from: [1] I. Chorkendorff and J. W. Niemantsverdriet, Concepts of Modern Catalysis and Kinetics. Weinheim: Wiley-VCH, 2006)

Moreover, the microstructures of the catalysts are dynamically changed when the catalysts are exposed to its real operating conditions, that are highly reactive environments due to gaseous and liquid reactants, heat, and etc.

In this regard, a comprehensive structural characterization, is highly required in the heterogeneous catalysis field. In 2014, Paul A. Midgley and Sir John Meurig Thomas introduced a new philosophy in materials characterization with a new term – Multi-dimensional electron microscopy (MEM),[3] in which a multi-dimensional dataset combining 3D real space morphology with temporal, chemical information is used for a new insight into the physicochemical behavior of materials. In the sense that heterogeneous catalysts have complicated three-dimensional shapes and its morphologies and chemical structures are continually varied, MEM is the right direction in characterizing as heterogeneous catalysts.

In this dissertation, within the philosophy of MEM, advanced transmission electron microscopy (TEM) techniques were developed and applied to address many practical and scientific questions behind heterogeneous catalysis. Among various problems in heterogeneous catalysts, the main focus is on the deactivation issue of heterogeneous catalysts due to nanoparticle sintering, as industries have to spend billions of dollars every year for replacement of catalysts.[4] In chapter 2.1, a new 3D electron tomography (ET) technique called the secondary-signal imaging electron tomography (SSI-ET) will be introduced and their operating mechanism will also be discussed.[5] It is expected that this technique will be highly useful to investigate the sintering behaviors of

the supported nanoparticles on a mesoscale oxide supports. In chapter 2.2, annular-dark field (ADF) scanning transmission electron microscopy (STEM) electron tomography (ADF-STEM ET) was applied to quantitatively characterize AuIr bimetallic catalyst to reveal the intrinsic high stability of the AuIr/TiO_2 catalyst.[6] In chapter 2.3, the *real-time* surface migration behavior, which is the most fundamental step of a sintering, of Ir atoms in the atomically dispersed Ir/MgO catalyst was investigated by using sequential Z-contrast AC-STEM[7] and the results will be discussed. Finally, in chapter 2.4, the MEM analysis which combines *in-situ* TEM (time), ADF-STEM ET (3D), *in-situ* EELS (spectral dimension) was performed to understand an unusual strong metal-support bonding behavior of Au-Fe_3O_4 dumbbell nanoparticles.

CHAPTER 2. DEVELOPMENT AND APPLICATION OF ADVANCED TRANSMISSION ELECTRON MICROSCOPY

2.1 A New Electron Tomography Technique in TEM for Mesoscale Specimens

Reproduced with permission from C. W. Han and V. Ortalan, "*Secondary signal imaging (SSI) electron tomography (SSI-ET): A new three-dimensional metrology for mesoscale specimens in transmission electron microscope*," *Micron*, 76, 62-67 (2015).

2.1.1 Introduction

With the development of the "Z-contrast electron tomography" utilizing incoherent and elastically transmitted electrons in a scanning transmission electron microscope (STEM) by Midgley and co-workers,[8,9] three-dimensional (3D) structure and morphology of crystalline materials have been successfully reconstructed with the spatial resolution of 1 nm^3.[10,11] However, the usefulness of the Z-contrast electron tomography has been limited to nanomaterials with relatively small thicknesses (~100 nm). Due to the contrast reversal,[12] the non-linear damping[13] of the intensities and the significant increase of inelastic scattering with the increasing thickness of the specimen, Z-contrast imaging of "ultra-thick" mesoscale specimens (a few μm) in conventional operating voltage TEM (e.g., 200 kV) fails to satisfy the projection requirement[14] for tomographic reconstruction.

Despite many efforts to overcome the thickness limitation, to the best of our knowledge, the reported values of maximum thickness of physical science specimen at which 3D imaging could successfully be performed in TEM have been below 1 μm.[12,15,16] Utilizing secondary signals for imaging and 3D tomographic reconstruction of ultra-thick samples with a TEM operating at conventional operating voltages (e.g., 200 or 300kV) was previously proposed.[17] More recently, it has been reported that secondary signal images taken in an SEM can be used to reconstruct 3D structure of micron-sized fiber systems.[18] In this paper, we have investigated underlying principles making the electron tomography of secondary signals in TEM viable and introduced a new electron tomography technique, so called the secondary signal imaging (SSI) electron tomography (SSI-ET), utilizing the secondary signals (secondary electrons (SE) and backscattered electrons (BSE)) in scanning-mode TEM as a novel 3D metrology for "ultra thick" mesoscale specimens. Moreover, we have investigated the applicability and limitations of the secondary signal based electron tomography in TEM on the basis of theoretical foundations (e.g., contrast mechanism of secondary signal imaging in TEM).

2.1.2 Methods

To demonstrate the capability of the SSI-ET, ZnO mesoneedle and mesotripod having mesoscopic dimensions (300 nm ~ 1.5 μm in diameter and ~5 μm in branch length) were investigated. TEM experiments, including bright-field TEM (BF-TEM) and SSI were performed using a 200 kV JEOL S/TEM microscope (JEM-2500SE) equipped with a scintillator type SSI (SE/BSE) detector. For tomographic reconstruction of the specimens, the SSI tilt series were acquired using 1◦ tilt angle interval over the range

−71◦ to +71◦ for the mesotripod and the range −69◦ to +69◦ for the mesoneedles. The acquired tilt series were reconstructed using the model based iterative reconstruction (MBIR) method in TEMBIR software.[19]

We also performed Monte Carlo (MC) electron scattering simulation using CASINO v3.2[20] to investigate the contribution (i.e., the relative amount) of SE and BSE in SSI with the purpose of interpreting the underlying mechanism of intensity and contrast of the acquired SSI images. In CASINO v3.2, the physical model for relativistic electron elastic cross-section (EECS) are implemented for 100–300 keV electrons[21] and therefore, the effects of the acceleration voltage of an electron beam and the thickness of ZnO on the BSE generation yield (η) and the SE generation yield (δ), defined as Eqs. (1) and (2), could be accurately investigated:

$$\eta = \frac{N_{BSE}}{N_{IE}} \quad \ldots (1)$$

where N_{BSE} and N_{IE} are the number of BSE and the number off incident electrons (IE), respectively.

$$\delta = \frac{N_{SE}}{N_{IE}} \quad \ldots (2)$$

where N_{SE} is the number of SE.

2.1.3 Results and Discussion

BF-TEM and SSI images of ZnO mesoneedle and mesotripod taken with 200 kV electron beam are shown in Fig. 2.1a, b and c, d, respectively. In the BF-TEM image (Fig.

2.1a) of ZnO mesoneedles (diameter: up to ~200 nm, length: up to ~1.5 μm) that are relatively thinner than the mesotripods, the thickness effect on contrast in BF image is clearly visible at the area at which two mesoneedles are stacked on top of each other (arrow in Fig. 2.1a). However, for the thicker ZnO mesotripod, diameter and length of each branch reaches up to about ~1 μm and ~6 μm, respectively and the BF-TEM imaging fails to project the thickness variation of the sample (Fig. 2.1b). Fig. 2.1b clearly demonstrates that imaging with transmitted electrons is not achievable for electron tomography of ultra-thick specimens with a microscope operating at conventional voltages. However, SSI images of the mesotripod remarkably show the thickness-dependent contrast (Fig. 2.1d). The locations (arrows in Fig. 2.1d), where a tripod and needles are overlapped, show higher intensity with compared to the intensity of the regions right beside the overlapped locations. SSI images of the ZnO mesoneedle show the thickness contrast (red arrow in Fig. 2.1c) as well.

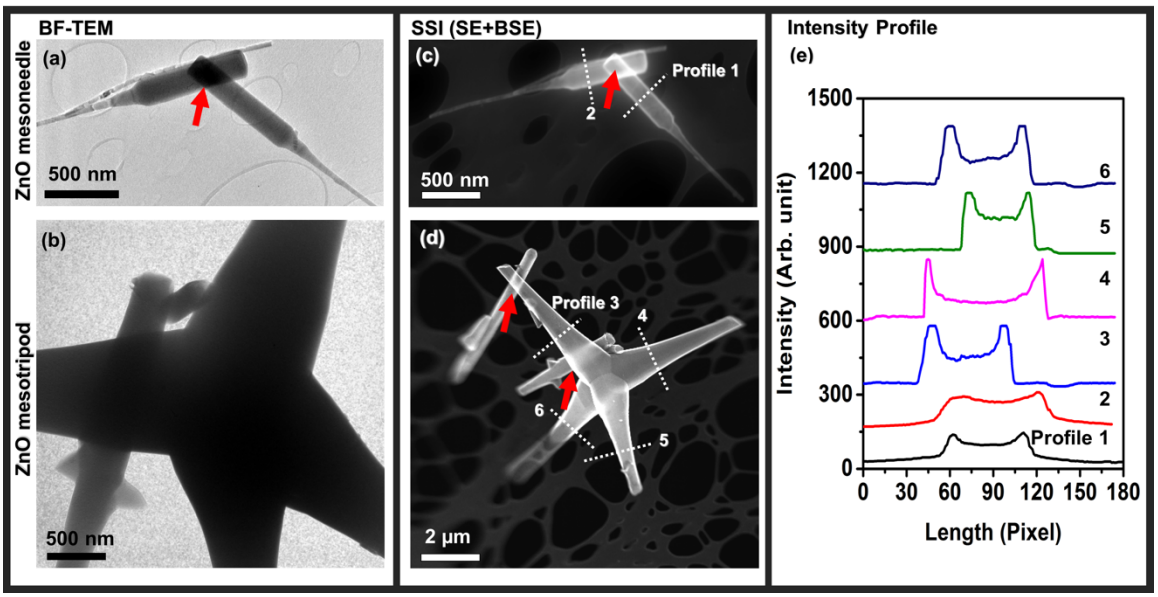

Figure 2.1. BF-TEM and SSI images of ZnO mesoneedle (a,b) and mesotripod (c,d) taken with 200 kV electron beam. The intensity profiles (e) along the lines annotated on Fig.1c and d.

Along with the thickness contrast, the strong intensity at the edge region is another feature of the SSI image of a mesoscale specimen (Fig. 2.1e). To reveal the origin of strong edge intensities, an SSI linescan simulation have been performed using CASINO v3.2 code (Fig. 2.2). In this simulation, 1µm thick ZnO slab was built to simulate the position dependency of SE and BSE generation in mesoscale specimens. Electron beam energy, probe size, and simulated number of electrons are 200 keV, 1 nm, and 30,000 electrons, respectively. A linescan profile was set across the boundary between vacuum and ZnO slab (Fig. 2.2a). Secondary yield plot (Fig. 2.2b) clearly shows that secondary electrons are more strongly generated at the edge than inner part of the ZnO slab. In contrast to SE, BSE yield does not show any position dependency (Fig. 2. 2c). Therefore, it can be concluded that the strong intensities (or bright edges) in SSI

images are originated from SE. The simulation results are also consistent with the fact that SE can only be emitted from the shallow surface due to the low energy of the SE.[22]

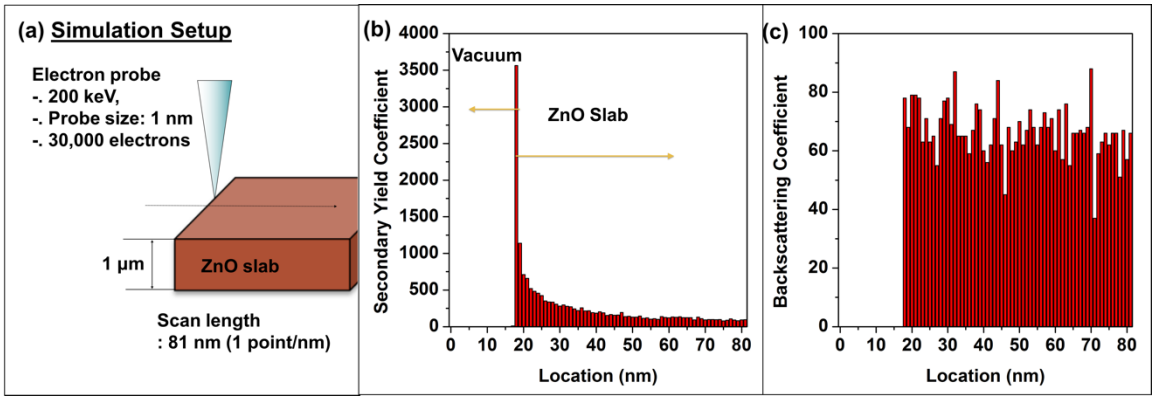

Figure 2.2 Results of the SSI linescan simulation. Schematic diagram describing the simulation setup (a), secondary yield coefficient (b), and backscattering coefficient (c).

The thickness contrast in the SSI images has not been demonstrated because the contrast of SSI in a scanning electron microscope (SEM) at the usual operating voltages (e.g., 10 and 25 kV) is usually dependent on the surface topology and/or atomic numbers (Z) of comprising elements (i.e., Z-contrast or mass contrast). Moreover, the contrast mechanism in atomic resolution SSI in STEM has been mostly attributed to SE emitted from a few atomic layers of the surface.[23,24] However, the SSI images collected from the ZnO tripod in STEM at 200 kV clearly indicate the thickness contrast, which cannot be explained by the contribution of SE.

To understand the thickness contrast observed in the SSI images, we performed a series of MC electron scattering simulations with varying sample thicknesses and primary electron energies. Fig. 2.3 shows that the SE yield and the BSE yield as a function of the ZnO thickness with different primary electron energy values. With the electron beam

energies in conventional SEM (e.g., 10 and 25 keV), the BSE yield is higher than the SE yield for the entire thickness range and the values of BSE and SE yield are nearly constant except submicron thickness range (Fig. 2.3a and b). The thickness contrast in SEM, therefore, is usually negligible. However, the thickness effect starts to become apparent as the incident energy of electrons exceeds 100 keV. In contrast to the SE yield, which is independent of the thickness, BSE yield shows a monotonic increase with increasing thickness of ZnO. At 100 keV, the BSE yield from 100 to 500 nm is lower than that of SE (~0.005). However, the BSE linearly increases up to ~0.25 with increasing ZnO thickness until the thickness of 15 μm at which the BSE yield is saturated (Fig. 2.3c). At 200keV, the BSE yield is negligibly low (0.0001) at 100 nm. This tells that if the specimen is thin (<100 nm), SE will be dominant in the secondary signals in STEM mode and this shows consistency with the experimental observation reported by Zhu *et al*. (2009). However, the BSE yield monotonically increases up to 0.138 at 35 μm with increasing thickness (Fig. 2.3d). Furthermore, the contribution of BSE in the secondary signal will be dominant with thick samples. More importantly, the change of BSE signals with varying thickness of ZnO satisfy the projection requirement,[14] that is the recorded signal should be a monotonic varying function of some physical property (here, the thickness) of a specimen. The thickness contrast induced by BSE enables 3D tomographic imaging of mesoscale materials in TEM and this contrast can only be obtained at high electron energies (100, 200 keV, or higher). From the results of MC electron scattering simulations, we found that the main contrast mechanism (that is, the major electrons contributing to the intensities) in SSI of the thick ZnO mesotripod specimens at 200 keV is the thickness contrast due to BSE.

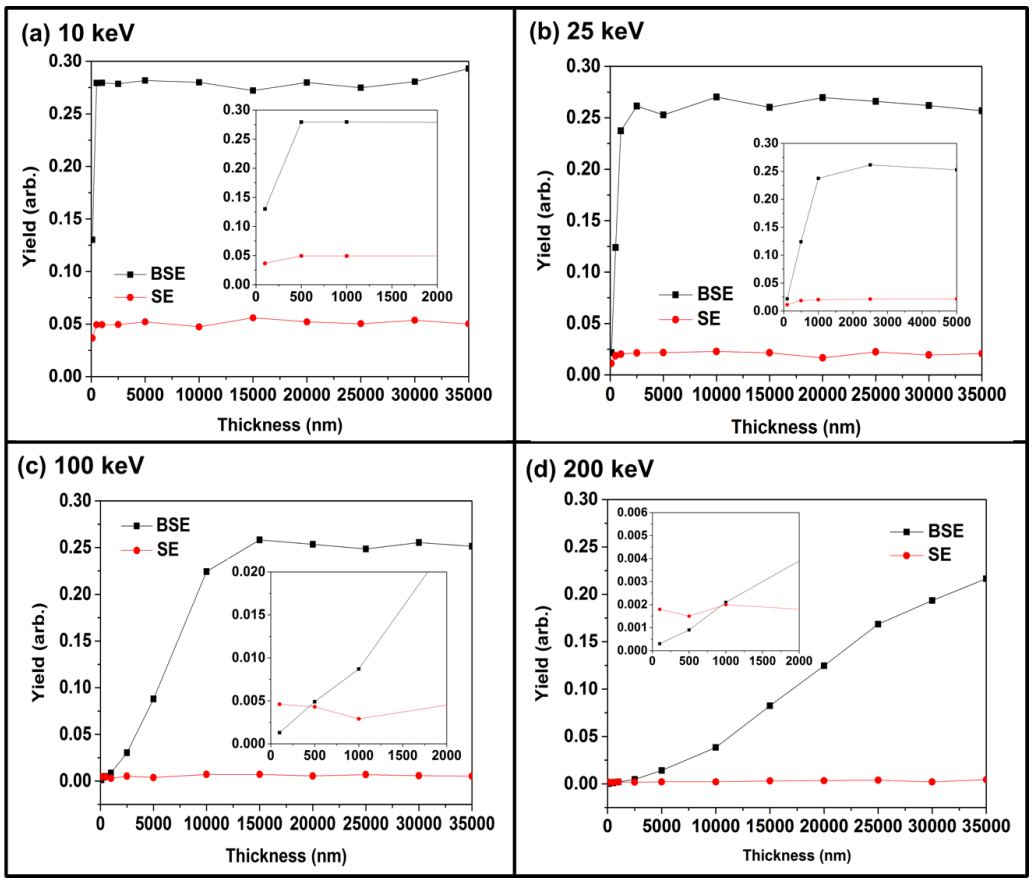

Figure 2.3 Variation of BSE and SE yield as a function of the ZnO thickness with primary electron energy values of (a) 10 keV, (b) 25 keV, (c) 100 keV, and (d) 200 keV.

In order to further investigate the contrast mechanism and the intensities of an image in the SSI in STEM at the most widely used 200 and 300 keV beams, a series of MC simulations were performed and the dependence of the BSE, the major signal in the SSI of thick samples with STEM, on atomic number (Fig. 2.4a and d) as well as the specimen thickness (Fig. 2.4b and e) were obtained. Fig. 2.4a and d shows the atomic number dependence of the BSE yields with varying thicknesses at 200 and 300 keV, respectively. In contrast to the monotonic increase of the BSE yield with increasing atomic number, which is generally observed in SEM, the BSE yields of the 200 and 300keV primary

electrons do not show the monotonic behavior over the entire atomic number range if the thickness of a specimen is thinner than 50 μm at 200 keV and 100 μm at 300 keV. The BSE yields of thinner samples satisfy the monotonic behavior for a certain range of the atomic number. As a consequence of this, the region showing the atomic number contrast (i.e., mass contrast) is limited as shown in Fig. 2.4c and f. Fig. 2.4b and e shows the thickness dependence of the BSE yields with varying atomic numbers at 200 and 300 keV, respectively. Both 200 and 300 keV beams show a common trend: relatively low atomic number elements (<20) show a monotonic increase of the BSE yield over the entire thickness range of the investigation and the BSE yield of the elements having high atomic number (>20) also shows a monotonic behavior, however it saturates if the thickness goes over the critical thickness (Fig. 2.4b and e). In general, the critical thickness values are inversely proportional to the atomic number. Based on these analyses, the region showing the thickness contrast is deter- mined (red region in Fig. 2.4c and f). Fig. 2.3c and f indicate the range of the atomic numbers and the thicknesses to which the SSI-ET is applicable. Considering the projection requirement for tomographic reconstruction, the shaded areas of thickness contrast (red regions in Fig. 2.4c and f) or mass-thickness contrast (purple regions in Fig. 2.4c and f) are the regions where the SSI-ET can be utilized. The contrast formation mechanism of the ZnO mesotripod used in this study corresponds to thickness contrast (filled ellipse in the red region in Fig. 2.4c). These atomic number-thickness maps of the contrast mechanism tell that the SSI-ET is readily applicable for ultra-thick (up to 50 μm at 200 keV and to 100 μm at 300 keV) single-phase specimens if those average atomic numbers are below 20.

Furthermore, the SSI-ET is also applicable for ultra-thick multi- phase specimens occupying the regions of mass-thickness contrast.

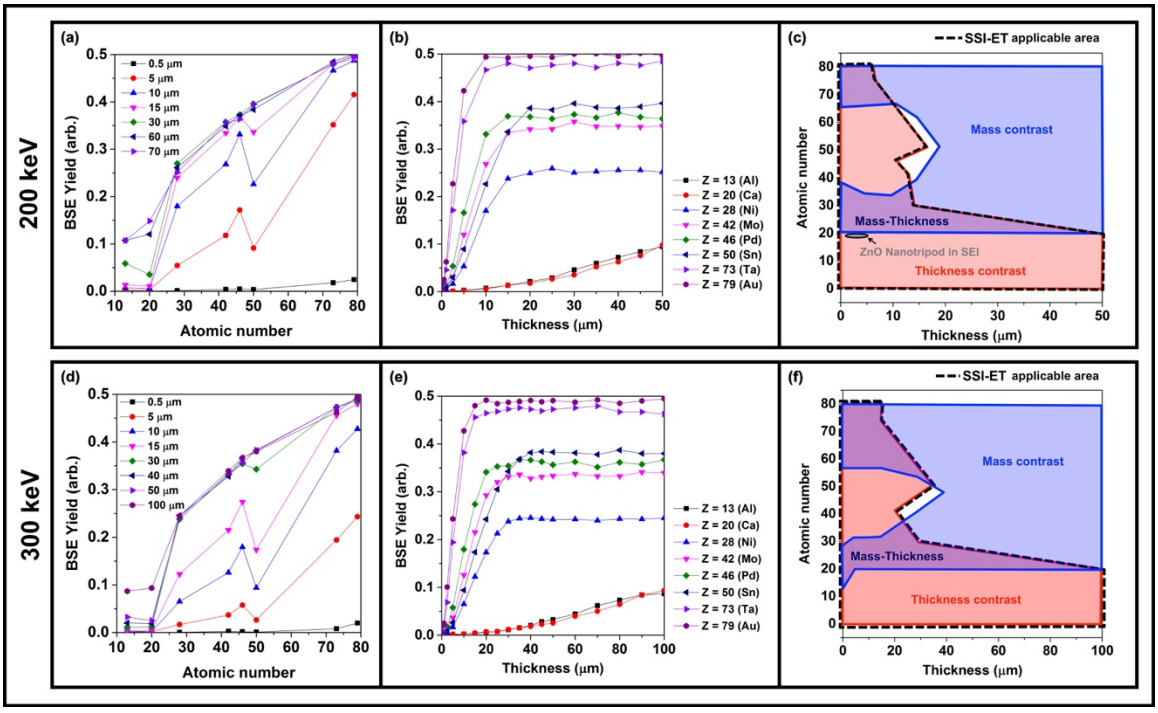

Figure 2.4 BSE yields as a function of the atomic number with various thickness values at 200 keV (a) and 300 keV beam (d), BSE yields as a function the sample thickness with different atomic number at 200 keV (b) and 300 keV (e), and atomic number-thickness map of the contrast formation mechanism at 200 keV (c) and 300 keV (f). The region to which the SSI-ET is applicable is surrounded with a dotted line.

Fig. 2.5 shows the SSI tilt series of the ZnO mesotripod, which was aligned by the fiducial marker alignment in IMOD software.[25] As it is suggested by the MC calculations, the thickness contrast can be clearly seen in this figure. The intensities of a branch of the mesotripod (red arrows) increase with increasing tilt angle. Since the effective thickness of ZnO along the optic axis (i.e., electron beam path in TEM) increases with tilting, the intensities of SSI image at higher tilt angles become stronger.

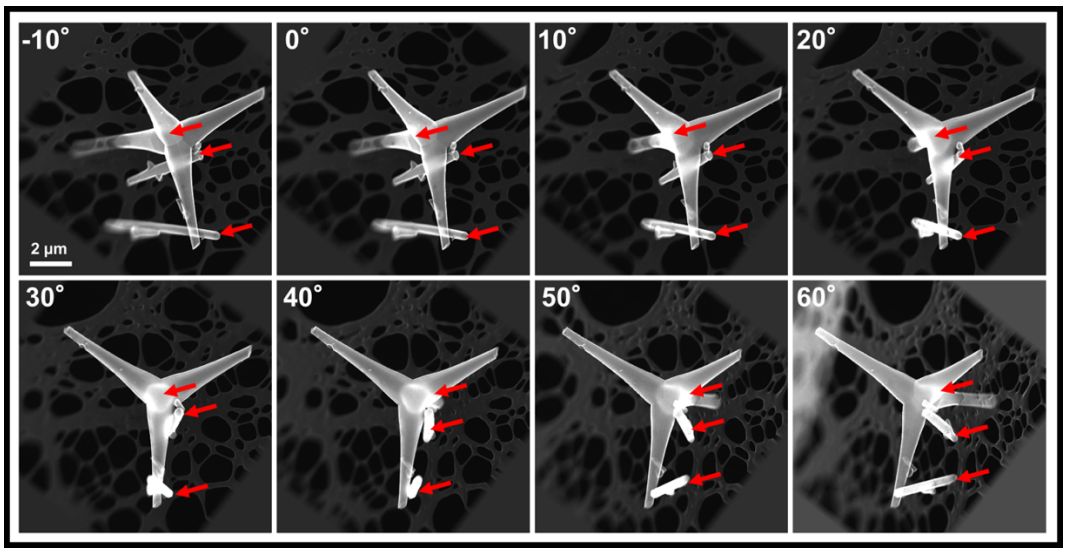

Figure 2.5 The SSI tilt series of the ZnO mesotripod, which was aligned by the fiducial marker alignment. Red arrows indicate the locations where the effective thickness along electron beam direction is increased with increasing the tilt angle. (For interpretation of the references to color in this figure legend, the reader is referred to the web version of this article.)

Volume-rendered SSI-ET tomograms of the ZnO mesoneedle and the mesotripod are shown in Fig. 2.6a and b, respectively. The reconstructed tomograms demonstrate the successful visualization of the 3D structure of mesoscale materials with SSI in TEM. Electron tomographic reconstruction in this scale is unprecedented, except the FIB tomography, which is usually useful for the densely packed bulk materials (e.g., a bulk piece of alloy) and not for freestanding complex structures. In this regard, SSI-ET opens up possibilities of correlative microscopy studies of materials in a single instrument with an extended range (i.e., from atomic scale to mesoscale). This is a marked advantage over synchrotron X-ray microtomography technique, which has been a major choice for mesoscale materials but its spatial resolution is limited to a few hundred nanometers.[26]

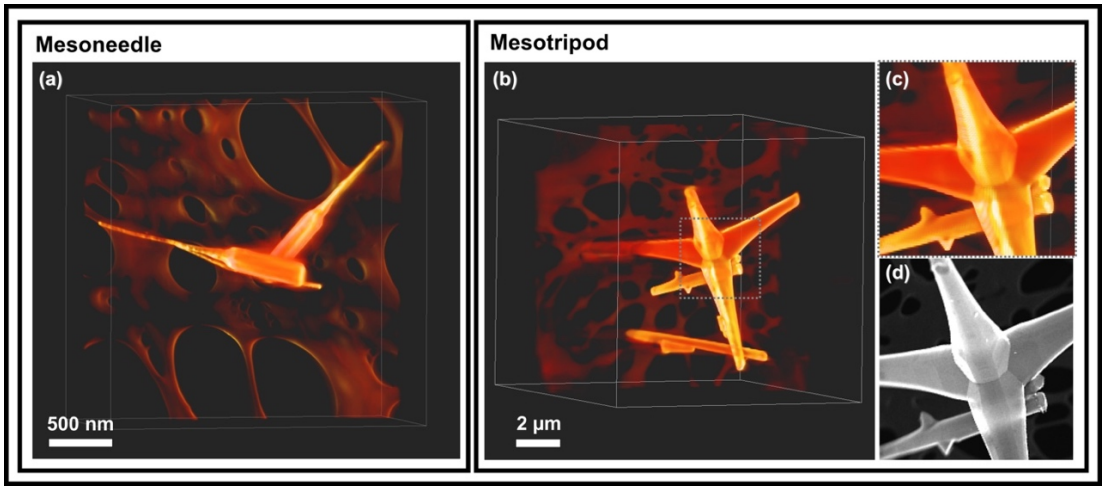

Figure 2.6 Volume-rendered SSI-ET tomogram of the ZnO mesoneedle (a) and the mesotripod (b). Detailed surface structures shown in the SSI-ET tomogram (c) and the SSI image (c). Tomogram Movies are available as supplementary information through Journal Micron website.

An interesting feature of the SSI-ET tomograms is the details at the surface region of the tomogram. In general, the STEM tomogram shows Z-contrast and therefore, the intensity of the volume-rendered tomogram will be uniform if the specimen is chemically homogeneous. In this case, an iso-surface rendering method requiring additional steps for segmenting voxels needs to be used to clearly see detailed surface features. On the contrary, the volume-rendered SSI-ET tomograms show higher intensities at the surface region than the inner part. More interestingly, the detailed surface structures, that are barely seen in the volume-rendered tomograms of any other “transmitted beam” based electron tomography, are clearly shown in the SSI-ET tomogram (Fig. 2.6c). The surface features of the tomogram are consistent with those shown in the SSI image (Fig. 2.6d).

Remarkable visibility of the surface features in the SSI-ET tomogram can be attributed to the contributions of the strong edge intensities due to SE. Although it has been known that signals violating the projection requirement cause artifacts in the tomographic reconstruction, the SE signal (i.e., strong edge intensities violating the projection requirement) enhances the visibility of the surface features in the SSI-ET tomogram. To demonstrate that strong edge intensities enhance visibility of the surface features in the SSI-ET tomogram, the SSI tilt series containing only edge intensities (Fig. 2.7a) was also reconstructed. Here, the SSI tilt series with edge intensities was obtained by the following procedure: A 5 × 5 Laplacian-of-Gaussian (LoG) filter was applied onto the original SSI images to detect edges. Then, the LoG filtered images were processed with a 5 × 5 dilation kernel and the results were binarized to get binary edge masks. Finally, the original SSI images were multiplied by the binary mask images. The reconstructed tomogram of the edge mask filtered SSI tilt series successfully represents the detailed surface structures (Fig. 2.7b), those are visible in the SSI- ET tomogram shown in Fig. 2.6. Similarly, it was reported that the tomographic reconstructions of edge-filtered images successfully visualized the surface structures of the specimen supporting that the utilization of SE can provide enhanced visibility of the surface features.[27] Depending on the relative importance of the surface structure, the emission of the SE to be collected by the detector can be suppressed by applying a positive bias on the specimen as previously demonstrated.[23,24]

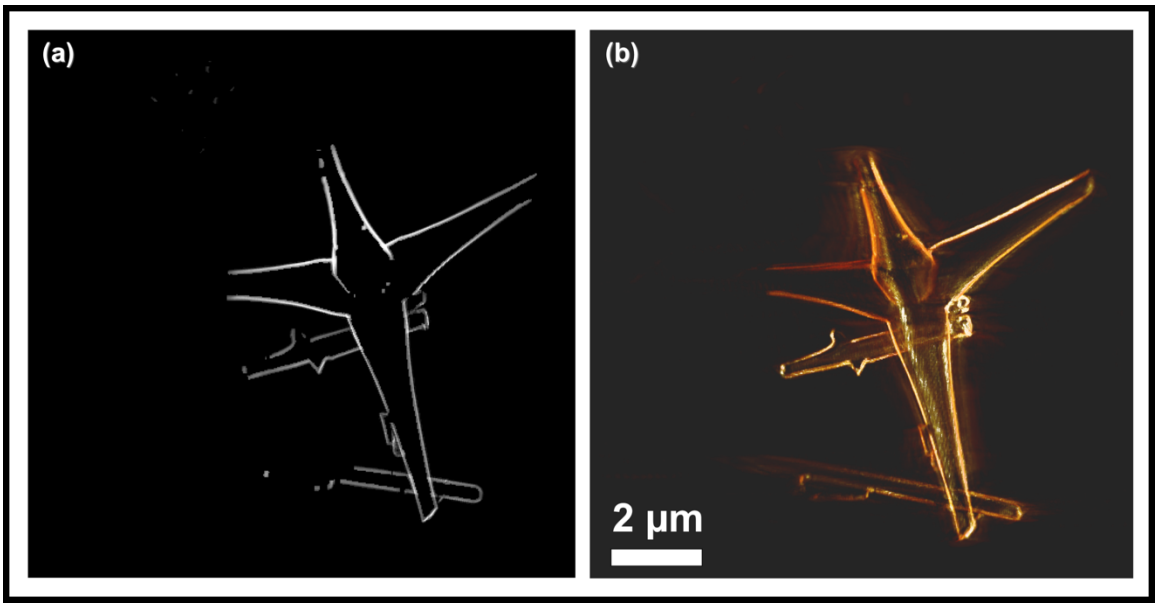

Figure 2.7 Edge mask filtered SSI image (a) and reconstructed SSI-ET tomogram of the mesotripod from the edge mask filtered SSI tilt series (b). Tomogram Movie is available as supplementary information through Journal Micron website.

2.1.4 Conclusions

We have demonstrated a new electron tomography technique using the secondary signals (SE and BSE) for mesoscale specimens. The MC electron scattering simulations revealed that the contrast mechanism in the SSI images of thick samples taken with 200 and 300 keV electron beam is the thickness contrast, which is contributed by the BSE. Along with the BSE generating the 3D volume information in the SSI-ET tomogram, the SE signal enhances the visibility of the surface features in the tomogram. Successful tomographic reconstruction using SSI proves that SSI-ET can directly be utilized for 3D structural analysis of mesoscale structures, those have never been characterized by electron tomography in TEM.

2.1.5 Supplementary Information

Tomogram movies are also freely available through the Journal Micron website at http://dx.doi.org/10.1016/j.micron.2015.04.013

Acknowledgements

We thank Purdue University and School of Materials Engineering for their generous start-up funding.

2.2 Z-Contrast STEM Tomography of AuIr Bimetallic Catalyst

2.2.1 Introduction

Since the discovery in the 1980's that supported Au nanoparticles have high catalytic activity for chemical reactions,[28,29] Au catalysts have attracted a significant amount of interest.[30] The exceptional low temperature activity of Au catalysts in the oxidation process makes them one of the most promising catalysts for greener chemical industries.[31–34] Despite the superior catalytic properties, however, inherent instability against sintering of Au nanoparticles,[35,36] which is the main reason for the loss of catalytic activity during catalytic reactions, hinders large-scale adoption in industry.[37] Therefore, developing a method to prevent the deactivation due to sintering is of the utmost importance in the field of Au catalysis.

Because metal particle growth is one of the most critical issues for many supported catalysts, studies on the methods for stabilizing such nanoparticles have widely been conducted. Common approaches include embedding nanoparticles into a matrix[38] and covering nanoparticles with porous thin oxides.[39–42] Despite the fact that those approaches successfully demonstrated that sintering of metal nanoparticles is mitigated

even at high temperature, implementation of said solutions are somewhat limited in that the catalytic activity is decreased. The reason for the reduced catalytic activity is that the active sites and/or diffusion of reactant molecules are limited due to the stabilizing materials that cover the metal nanoparticles and supports.[43,44] Furthermore, the approach to encapsulate individual metal particles with porous shells may be challenging for large-scale production.[45]

There have been a significant number of investigations on stabilization via physical confinement, however, stabilization studies based on engineering the composition of the metal nanoparticles are limited thus far. Although there are abundant reports on controlling the composition of nanoparticles comprising a second metal, the main focus in those reports was to tailor their catalytic activity and selectivity.[46,47] Recently, Cao and Veser reported that the stability of Pt nanoparticles can be significantly increased when Pt nanoparticles are alloyed with Rh.[48] Given the fact that bimetallic catalysts with high stability don't require special synthesis processing for stabilization, their utilization as industrial catalysts is of great interest.

There are a few reports on the increased stability of Au catalysts by adding a second metal.[374950515253] In the Au-based bimetallic catalysts (e.g., AuIr, AuAg and AuCu), the enhanced thermal stability of supported metal nanoparticles is explained by the existence of a second metal oxide phase (IrO_2, AgO, and CuO) that provides stronger adhesion for the active metal nanoparticles onto the primary oxide support than those without having the secondary metal oxide. However, we recently found that the bimetallic AuIr/TiO_2 catalyst synthesized by sequential deposition-precipitation method of Au and Ir maintains small particle size even after reduction heat-treatment at 500 °C in

H_2 (hereafter, referred to as activation or activation heat treatment). This was unexpected because the previous H_2 temperature programmed reduction (H_2-TPR) study revealed that the IrO_2 phase is reduced below the activation temperature[49] and therefore, the stabilization effect due to IrO_2 is not expected to exist. This result convinced us that another mechanism plays a role in the stabilization effect in AuIr/TiO_2 bimetallic catalyst.

To understand the properties of supported catalysts, sophisticated structural characterization techniques are indispensable. Transmission electron microscopy (TEM) has been key for investigating the local atomic structure of metal nanoparticles and supports. Especially, aberration-corrected scanning transmission electron microscopy (STEM) utilizing a sub-Ångstrom electron probe provides unprecedented spatial resolution in terms of imaging and chemical analysis.[54,55] Despite being a powerful technique for atomic-scale characterization, in most cases, two-dimensional (2D) TEM projection images are not sufficient to investigate three-dimensional (3D) structures.[9,56] When considering that industrial heterogeneous catalysts have complicated 3D morphologies and that this significantly affects the properties of catalysts, such as activity, stability and selectivity, 3D characterization is critical and should be combined with 2D atomic-resolution studies.

High-angle annular dark-field (HAADF) Z-contrast STEM tomography opens the possibilities to characterize 3D structures of various nanostructured materials with nanoscale spatial resolution.[8–11,57] This technique has been successfully utilized for heterogeneous catalysts.[58,59] 3D information obtained by HAADF-STEM tomography, such as the spatial distribution of metal nanoparticles and morphologies of catalysts and supports, provides valuable insights into catalysis.

Furthermore, given that 3D information is key to understand the stability of catalysts,[44] HAADF-STEM tomography also provides a powerful tool for probing the atomic-level mechanisms of catalyst degradation.

In this study, we performed a wide variety of transmission electron microscopy analysis and computational techniques combining quantitative HAADF-STEM tomography, aberration-corrected HAADF-STEM imaging/spectroscopy, and density functional theory (DFT) calculations to investigate the enhanced stability of AuIr/TiO_2. Quantitative results of 3D spatial distributions and individual locations of AuIr nanoparticles, which are critical to reveal the mechanism behind the enhanced stability of AuIr bimetallic catalysts, were obtained. Moreover, aberration-corrected STEM imaging and X-ray energy dispersive spectroscopy (XEDS) were combined to investigate atomic resolution morphologies and chemical compositions that are not readily accessible in electron tomography. Finally, DFT calculations were performed to quantify the strength of adhesion between AuIr layers of various compositions and the anatase-TiO_2 support.

2.2.2 Methods

A bimetallic AuIr/TiO_2 (experimental loading 2.8 wt% Au, 2.7 wt% Ir) catalyst was synthesized by sequential deposition-precipitation with urea (DPU) method as previously reported. Ir nanoparticles were first deposited on Degussa (now Evonik) P25 TiO_2 by the DPU method. Ir/TiO_2 sample was washed and dried at 80 °C in vacuum for 2 h and calcined in air at 500 °C for h. Next, Au was deposited onto calcined Ir/TiO_2 sample by DPU method. AuIr/TiO_2 sample was washed and dried at 80 °C in vacuum for 2 h. The activation heat treatment, which has an effect on increasing the catalytic activity

and selectivity of AuIr/TiO_2, was performed in H_2 at 500 °C for 2 h. For the activation, the temperature was intentionally chosen to fully reduce IrO_2 for the purpose of investigating the role of IrO_2 in the stabilization of AuIr nanoparticles. For comparison, monometallic Au/TiO_2 synthesized also by the DPU method and activated under the same conditions were studied as well (i.e., 500 °C in H_2).

Aberration-corrected HAADF-STEM imaging and STEM-XEDS analysis were performed using a probe-corrected FEI Titan 80-300 STEM and a JEOL ARM200CF. Three-dimensional characterization of AuIr/TiO_2 and Au/TiO_2 was performed by HAADF-STEM tomography. Three sets of tilt-series (one from AuIr/TiO_2, one from Au/TiO_2, another tilt series from Au/TiO_2 at low magnification) were collected with the tilt range of at least ± 60 °C on an FEI Titan 80-300 S/TEM. The tilt series were aligned utilizing cross-correlation, which was followed by fine fiducial marker alignment. Aligned tilt series were reconstructed using TEMBIR method.[19] Reconstructed tomograms were surface rendered and segmented by Avizo software.

All DFT calculations were performed using the Vienna Ab-initio Simulation Package (VASP)[60] which implements the projected augmented wave approach (PAW).[61] GGA-PW91 was used for the treatment of exchange correlation energies.[62] The TiO_2 support was modeled with (101) surface of anatase, which is known to be the most stable surface.[63] The vacuum layer between the slabs was fixed at 25 Å. A Monkhorst-Pack scheme with 2x2x1 k points was used to sample the Brillouin zone. Tests with a denser k-point grid confirm convergence with respect to k-points. Electronic tests were converged to $1.0x10^{-4}$, and ionic steps were converged to a force of 0.02 eV/Å. The energy cutoff

was fixed at 400 eV, and a Methfessel-Paxton smearing of 0.1 eV was employed for the slab surfaces. The adhesion energy of the slabs (E_{ad}) on TiO_2 was calculated as

$$E_{ad} = E_{slab+TiO_2} - E_{slab} - E_{TiO_2} \quad \ldots \text{Eq}$$

where $E_{slab+TiO2}$ is the energy of the slab supported on TiO_2, E_{slab} is the energy of the slab in the gas phase, and E_{TiO2} is the energy of the anatase TiO_2 support.

2.2.3 Results and Discussion

Figure 2.8 shows the results of characterization for as-prepared and activated AuIr/TiO_2 and Au/TiO_2 by HAADF-STEM imaging and HAADF-STEM tomography. The first and second row of Fig. 2.8 represent the results obtained from AuIr (a-c) and Au samples (d-f), respectively. The first and second columns show HAADF-STEM images of as-prepared and activated samples. In HAADF-STEM images, high-Z elements, Au (Z=79) and Ir (Z=77), have high intensity, and the low-Z TiO_2 support (Z=12.7 in average) has relatively low intensity when compared to the metal nanoparticles. The third column of Fig. 2.8 shows the surface-rendered tomograms obtained by reconstructing the HAADF-STEM tilt series. In the tomogram, AuIr and Au nanoparticles are colored red and yellow, respectively. The surface-rendered TiO_2 support has transparency for better visibility of the metal nanoparticles. The histogram in Fig. 2.8 illustrates the measured metal particle size distributions. As shown in the first column of Fig. 2.8, as-prepared AuIr (Fig. 2.8a) and Au (Fig. 2.8d) are quite similar (Au: 0.96 ± 0.13 nm, AuIr: 0.96 ± 0.17 nm) in terms of the size of metal nanoparticles on the support. However, the size distribution and morphologies of AuIr (Fig. 2.8b) and Au (Fig. 2.8e) after the activation process are clearly different from each other. Despite the activation heat-treatment, AuIr

bimetallic nanoparticles maintained a small average size (2.65 ± 1.07 nm in diameter) and dispersed uniformly on the TiO_2 surface. Furthermore, AuIr particles have a homogeneous size distribution (Fig. 2.8g, red columns). In contrast to the bimetallic case, Au/TiO_2 reduced in the same condition shows that Au nanoparticles were significantly sintered with considerably larger average size (5.32 ± 3.28 nm in diameter) than that of AuIr nanoparticles, as shown in the STEM image (Fig. 2.8e) and the reconstructed tomogram (Fig. 2.8f). In addition, the size of Au nanoparticles has a much wider distribution (Fig. 2.8g, yellow columns) than that of bimetallic AuIr (i.e., inhomogeneity in particle size).

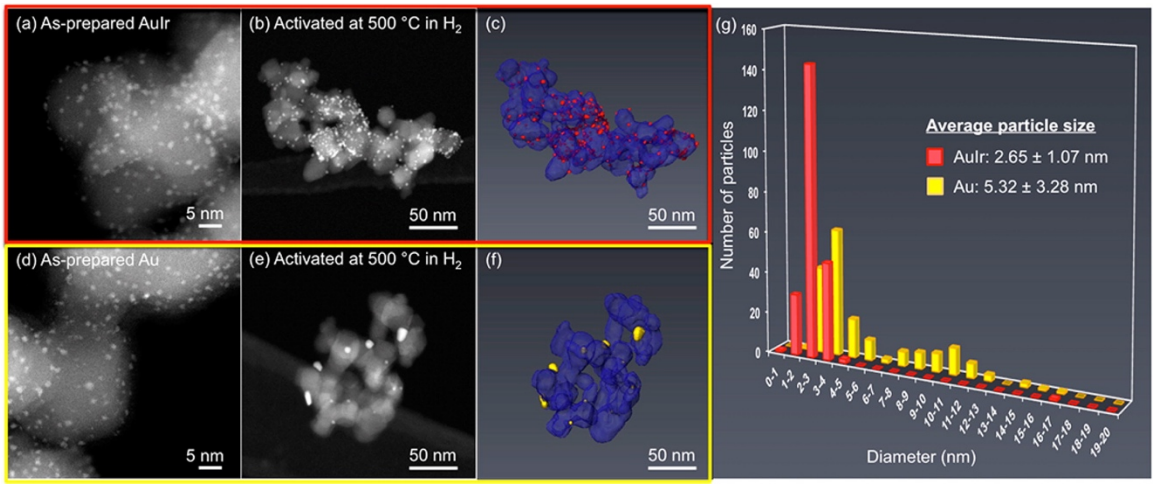

Figure 2.8 Structures of AuIr and Au on TiO_2 shown in HAADF-STEM images and STEM tomograms. Representative HAADF-STEM images for (a) as-prepared AuIr/TiO_2 and (b) activated AuIr/TiO_2. (c) Surface-rendered tomogram for AuIr/TiO_2 showing AuIr nanoparticles colored red and TiO_2 support colored semitransparent blue. Representative HAADF-STEM images for (d) as-prepared Au/TiO_2 and (e) activated Au/TiO_2. (f) Surface-rendered tomogram for Au/TiO_2 showing Au nanoparticles colored yellow. (g) Histogram of particle size distributions of AuIr (red) and Au (yellow).

Our investigations showed that sintering of the AuIr nanoparticles was reduced significantly due to the presence of Ir during the activation heat-treatment condition, in which it has been known that any IrO_2 would be reduced, and therefore the so-called "nanoglue" effect[64] of IrO_2 cannot exist. To confirm that there is no "locally remaining" IrO_2 phase affecting the stability of the AuIr nanoparticles, we utilized atomic resolution aberration-corrected HAADF-STEM imaging to investigate the interface between the AuIr nanoparticles and TiO_2. Typical edge-on view images of AuIr/TiO_2 confirm that there exist no other phases except bimetallic nanoparticles and TiO_2 (Fig. 2.9a). This finding leads us to posit the hypothesis that AuIr nanoparticles are intrinsically stable instead of being stabilized with the help of the second metal oxide phase (i.e., IrO_2) at the nanoparticle/support interface. We also performed XEDS linescan analysis to determine how the different metal atom species in AuIr bimetallic nanoparticles distributed within the nanoparticle interior and at the nanoparticle surfaces (random alloy, core-shell, or separate phases) (Fig. 2.9b). The result shows that AuIr nanoparticles are not core-shell or separate Au and Ir particles but random alloys suggesting that AuIr nanoparticles can have high stability intrinsically with the mixed alloy structure.

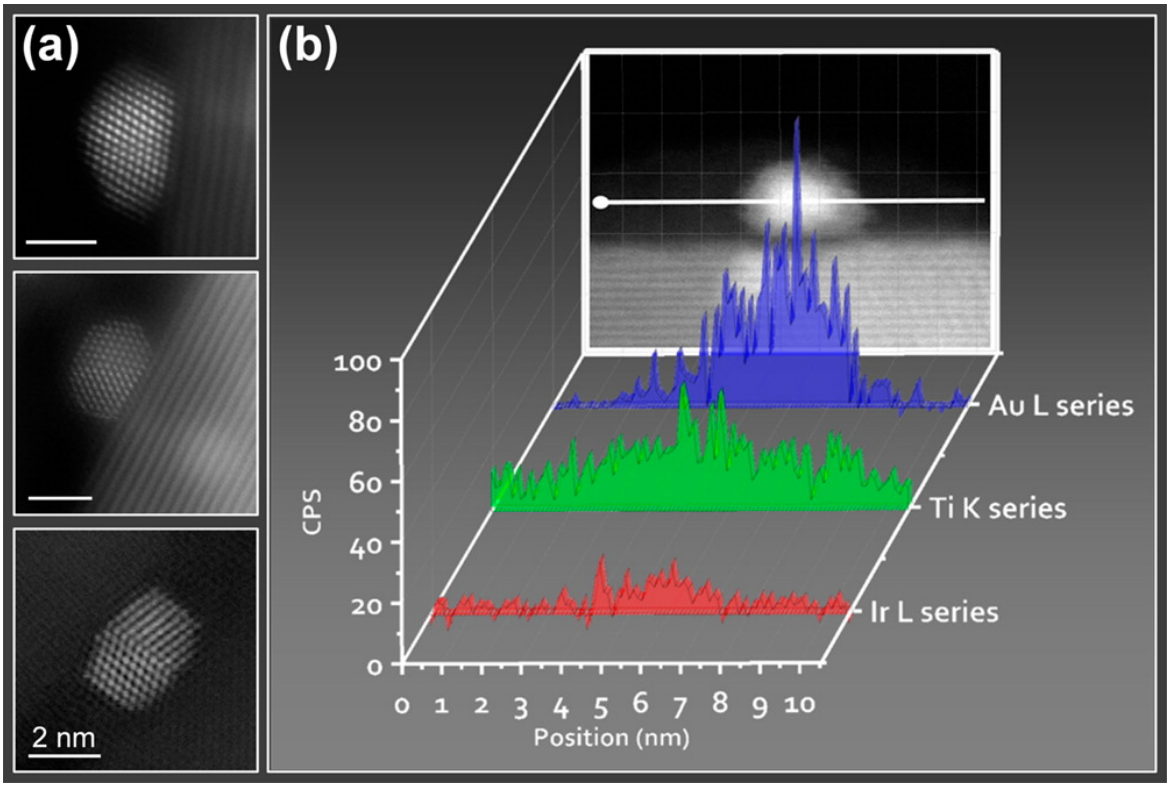

Figure 2.9 Representative atomic structures and chemistry of AuIr/TiO_2. (a) Aberration-corrected HAADF STEM images showing representative AuIr nanoparticles attached on TiO_2 support. (b) STEM-XEDS line-scan profiles for AuIr nanoparticles. Z-contrast images are smoothed for better visualization.

Besides high resolution analysis of a single nanoparticle, HAADF-STEM tomography can be utilized to understand stability of supported catalysts[45] because electron tomography provides the stability-relevant 3D structural information, such as nearest-neighbor distances between metal particles and anchored locations of the metal particles on supports.

The nearest-neighbor distance between the active metal nanoparticles is an important factor that needs to be considered to understand the sintering behavior and the stability of the catalyst due to the fact that mass transport through surface diffusion and/or migration of the particle will be facilitated if the distance between particles is shortened.[45,65] Figure 2.10a shows the distribution of nearest-neighbor distance for Au and AuIr. Due to the sintering of Au nanoparticles during the reduction heat treatment and the resultant reduction in number of Au particles, the nearest neighbor distance between Au nanoparticles was significantly increased (average: 41.04 ± 15.83 nm). Therefore, it is expected that further growth in particle size was prohibited due to the large nearest-neighbor distance. On the other hand, AuIr nanoparticles maintained a short distance between the nearest neighbors (average: 7.23 ± 3.86 nm) with a narrow distribution even after the activation. It is remarkable that AuIr didn't grow further in size and maintained stability despite their spatial distribution with short nearest-neighbor distance. The results can be understood if one assumes that the AuIr nanoparticles on TiO_2 have intrinsically lower free energy than that of Au on TiO_2, in which case, the thermodynamic driving force for sintering of AuIr will be naturally lower than for monometallic Au.

The locations at which AuIr nanoparticles are anchored on TiO_2 also indicate intrinsic lower free energy for AuIr/TiO_2 (Fig. 2.10b). Energetically, TiO_2 grain boundaries (GB) and/or local rough surfaces (RS) are preferred locations for reducing the total free energy of the catalysts. In this aspect, it is expected that metal nanoparticles will be more frequently found at the TiO_2 GB/RS than on TiO_2 smooth surfaces (SS). However, AuIr particles are uniformly distributed on the TiO_2 surface as shown in Fig.

2.10b. To investigate the locations of individual AuIr nanoparticles in a quantitative manner, the TiO_2 surface was categorized as "GB/RS" and "SS" as illustrated in the inset of Fig. 2.10b. Locations of each single metal nanoparticle were determined from the surface-rendered tomogram of Au/TiO_2 (of lower magnification for statistical analysis) and AuIr/TiO_2. About 90 % of Au nanoparticles are located on the TiO_2 GB/RS and only 10% are on the SS suggesting that the high thermodynamic driving force for sintering of Au nanoparticles on TiO_2 leads to most of the Au nanoparticles to be located on the TiO_2 GB/RS. This tendency shows consistency with the previous report on the Au/TiO_2 catalyst.[66] In the case of AuIr/TiO_2, the tendency to be located on the TiO_2 GB/RS is considerably reduced as compared to the case of Au. More uniformly distributed AuIr nanoparticles on TiO_2 manifests that the thermodynamic driving force to reduce the free energy (i.e., driving force to be located on the GB/RS) of the AuIr/TiO_2 is considerably weaker than that of Au/TiO_2. This low driving force also indicates that AuIr/TiO_2 has intrinsically lower free energy.

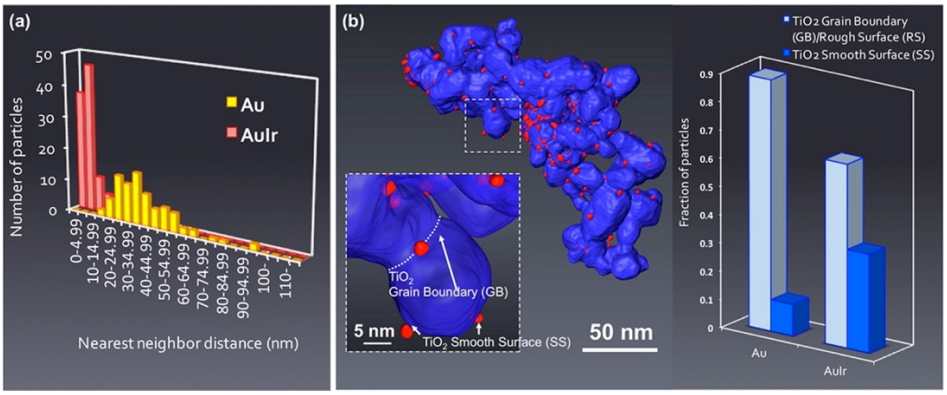

Figure 2.10 Quantified three-dimensional structures of AuIr/TiO_2. (a) Histogram showing the nearest-neighbor distances between metal nanoparticles of Au (yellow) and AuIr (red). (b) Tomogram showing typical surface morphologies of TiO_2 support and histogram showing fractions of the locations of metal nanoparticles of Au and AuIr on TiO_2 support.

Although the 3D information collected by HAADF-STEM tomography reflects that AuIr/TiO_2 has lower free energy compared to Au/TiO_2, the physical origin of the lowered free energy of the AuIr catalyst cannot be readily determined from TEM analysis. Therefore, we performed theoretical DFT calculations to further explore the molecular foundations of the enhanced stability of the AuIr/TiO_2. As described further in our DFT analysis (see below), the increased adhesion energy between AuIr particles and the titania supports is likely to suppress diffusion and aggregation of the AuIr particles across the TiO_2 surface.

DFT calculations are carried out on the (101) surface of anatase TiO_2. The surface termination of TiO_2 is shown in Fig. 2.11a, with under-coordinated O atoms (O 2c) and Ti atoms (Ti 5c). This surface termination is frequently used for anatase computations. Segregation studies were done on fcc (111) surfaces of five layered AuIr slabs with an overall composition of 1:1. This slab thickness is sufficiently large to capture trends in segregation energetics, which are the primary focus of this study. The bulk lattice constant of AuIr was computed to be 4.02 Å, which lies between the lattice constants of Ir (3.88 Å) and Au (4.17 Å). These values agree with experimentally and theoretically reported lattice constants of Ir (3.83 Å)[67] and Au (4.08 Å).[68] While the experimental system consists of AuIr nanoparticles dispersed on TiO_2, we used slab models to obtain insights into segregation behavior; such models are generally appropriate for nanoparticles with diameters of more than a few nanometers.[69] The slabs were supported on a three layer thick (101) anatase surface. The bottom layer of the TiO_2 slab was passivated using hydrogen to compensate for the effect of dangling bonds. Such an approach is often used to perform first principle calculations for semiconducting oxide

surfaces. We note that, while the magnitude of the adhesion energies was affected by hydrogen passivation, the relative trends did not change. To minimize strain between the AuIr and TiO_2 substrate, 4x4 AuIr slabs on 4x3 TiO_2 unit cells were employed. All atomic layers in the system were fully relaxed.

Figure 2.11b1-b6 shows relaxed configurations of AuIr slabs with typical Au and Ir segregation patterns that have been tested in this study. Corresponding segregation energies (SE) and adsorption energies (AE) for each configuration are also reported in Fig. 2.11b. Configuration in Fig. 2.11b1 shows the unsegregated slab, Fig. 2.11b2 shows a configuration with Au segregated to both top and bottom surfaces with associated Ir segregation to the adjacent layers, and configurations shown in Fig. 2.11b3-b6 depict slabs with different degrees of Ir segregation to the bottom layer. In all cases, the middle layer in the slab was kept at a 1:1 composition of Au:Ir, to mimic 1:1 bulk alloy. For given configurations of segregated slabs – Fig. 2.11b3-b6, we examined multiple configurations by changing the coordination environments of Au and Ir atoms in the bottom two layers and report those that we have found to have the lowest energy. All SEs are referenced to the unsegregated slab depicted in Fig. 2.11b1. Clearly, complete Au segregation to both surfaces is the most stable slab configuration in the absence of a TiO_2 support. Hence, to study the effect of slab adsorption on TiO_2 on the calculated segregation profiles, all segregated slabs were required to preserve a top layer of pure Au (Fig. 2.11b). We note that the adsorbed slabs have a residual strain of 6 % compared to the anatase substrate; this strain may, in part, be responsible for the relaxations seen in Fig. 2.11b.

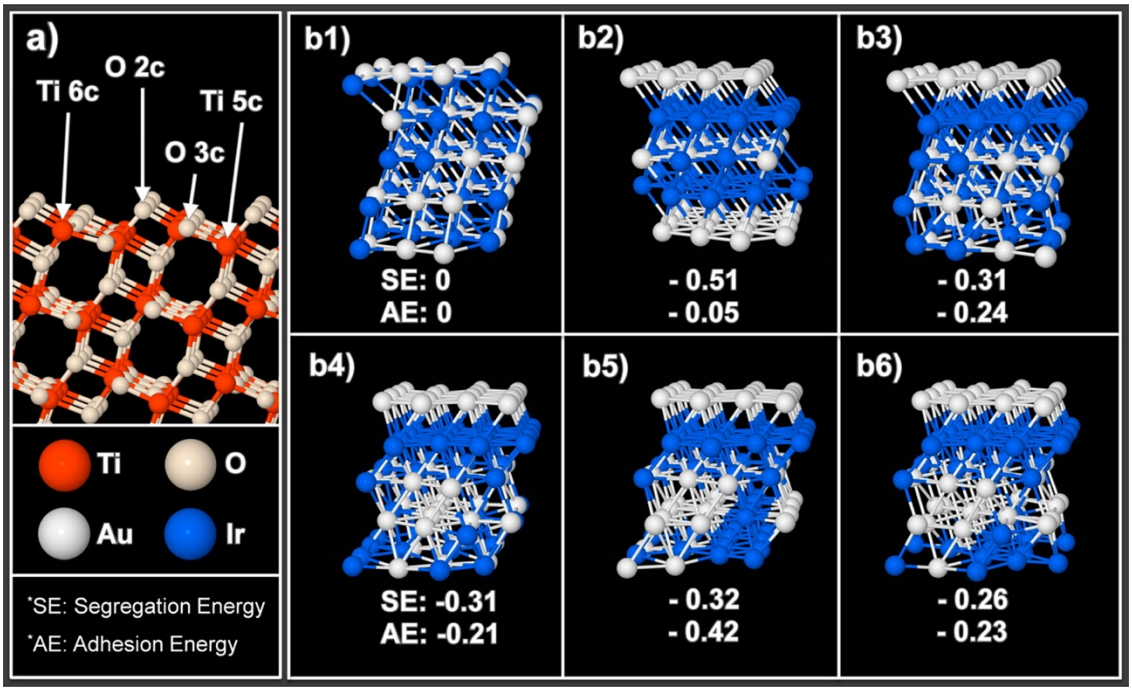

Figure 2.11 Atomic configurations of calculated anatase surface and AuIr slabs. (a) (101) surface structure of anatase TiO_2. (b) Structures of AuIr slabs: (b1) Configuration of 1:1 composition throughout, (b2) Au segregated to both surfaces, (b3-b6) Slabs with Au segregated to the top and increasing Ir composition in % in the bottom layer: (b3) 50 (b4) 62.5 (b5) 75 (b6) 87.5 (Unit of SE and AE: eV/AuIr pair and eV/surface Ti atom, respectively).

The AEs of all the slabs when supported on TiO_2 on a per surface Ti atom basis are also reported in Fig. 4b. It is seen that a pure Au layer in contact with the anatase has the weakest adhesion of all the configurations. As the amount of Ir in the bottom layer increases, the adhesion of the slab on TiO_2 becomes stronger. The adhesion is strongest for configuration shown in Fig. 2.11b5, with 75% Ir in the bottom layer, beyond which we see a weakening in adhesion in config. in Fig. 2.11b6, although it is still more stable than config. in Fig. 2.11b2 with pure Au at the bottom. These results suggest that

stabilization occurs as more and more bonds form between the Ir and the TiO_2 substrate. However, beyond a certain Ir concentration in the bottom layer, all oxygen atoms on the anatase surface are saturated by Ir, and any additional Ir does not lead to extra stabilization. These results indicate that if Ir is present close to TiO_2 in the AuIr nanoparticles, it will increase the strength of adhesion of nanoparticles to the substrate, likely resulting in reduced diffusion of the particles across the surface and reduced sintering by migration and coalescence. Furthermore, increased strength of adhesion between metal particles and supports lowers free energy of the catalyst and as a consequence of that, sintering by Ostwald ripening mechanism can also be effectively suppressed.[70] As described above, our experimental synthesis of the nanoparticles was done such that Ir was deposited first on the anatase, with Au subsequently deposited. This procedure is consistent with the presence of some Ir atoms at the interface with the anatase. Crucially, however, this mechanism does not rely on the presence of a fully developed iridium oxide; simple presence of Ir at the interface is sufficient to enhance the system stability.

The results of our investigations on AuIr/TiO_2 using quantitative HAADF-STEM tomography, imaging and spectroscopy consistently indicate an intrinsic low free energy of AuIr bimetallic nanoparticles on anatase TiO_2. Furthermore, theoretical DFT calculations reveal that the adhesion energy, a major determining factor for stability, can be enhanced when Ir atoms are added to Au nanoparticles and Ir atoms are segregated towards the AuIr/TiO_2 interface. These results indicate that stabilization of AuIr catalyst does not originate from the existence of a secondary oxide phase (i.e., IrO_2) but rather its

origin resides on the interfacial electronic effects. More importantly, the result of the DFT calculations strongly suggests that the metal deposition sequence in preparing bimetallic catalyst could be a critical factor, considering the fact that Ir atoms should be segregated near TiO_2 surface to increase the adhesion energy.

2.2.4 Conclusions

Bimetallic AuIr and monometallic Au catalysts on TiO_2 were investigated using quantitative HAADF-STEM tomography, aberration-corrected STEM imaging, STEM-XEDS, and DFT calculations to reveal the origin of the increased stability of the bimetallic AuIr catalyst. We have obtained three-dimensional structural features including nearest-neighbor distances between AuIr particles and anchored locations of the AuIr particles. Aberration-corrected STEM images confirmed that there exist no IrO_2 phase at the interface between the AuIr nanoparticles and TiO_2. Furthermore, STEM-XEDS revealed that AuIr nanoparticles are in the form of mixed alloy. The results lead to the conclusion that AuIr/TiO_2 has intrinsically low free energy preventing sintering. A series of DFT calculations and configuration models explain the free energy reduction of AuIr/TiO_2 when compared to Au/TiO_2: namely, the addition of Ir atoms into Au nanoparticles improves the adhesion energy of the AuIr nanoparticles to anatase TiO_2 surfaces, and as a consequence, the free energy of the catalyst and thermodynamic driving force to sintering is significantly lowered. These experimental and theoretical results show the possibility of improving the stability of supported Au nanoparticles and other supported metal catalysts by introducing suitable elements into the nanoparticles during the synthesis processes. This is of considerable interest to the heterogeneous

catalysis industry by virtue of the readily implementable synthesis technique in large-scale production. Furthermore, when considering that nanostructures are indispensable building blocks for advanced energy storage materials, engineering the free energy by alloying or doping can be expected to play a significant role in improving the performance of the materials that are critical to solve energy and environment related issues.

2.2.5 Supplementary Information

Methods

HRTEM and HAADF-STEM imaging for particle size measurement

The high-resolution transmission electron microscopy (HRTEM) imaging and high-angle annular dark-field (HAADF) STEM imaging were performed at 300 kV using an FEI Titan 80-300 microscope at the Birck Nanotechnology Center, Purdue University and FEI Titan S 80-300 probe corrected microscope at Oak Ridge National Laboratory. The microscopy images acquired from the bimetallic AuIr and monometallic Au supported on TiO_2 characterize the steady state (long-term) stability of the catalyst samples. Particle size measurements for AuIr nanoparticles and Au nanoparticles were performed using the ImageJ software from the collected HRTEM and HAADF-STEM images.

HAADF-STEM Tomography

Two HAADF-STEM tilt series and one tilt-series were collected from the Au/TiO_2 and $AuIr/TiO_2$ using an FEI Titan 80-300 microscope at the Birck Nanotechnology Center, Purdue University. Since Au nanoparticles were highly sintered, the number of Au nanoparticles found at high magnification tilt-series was too low to get a good statistic information. Therefore, we collected a low magnification tilt-series from the Au/TiO_2 having enough number of Au nanoparticles. The collected HAADF-STEM tilt series were aligned by the fiducial marker alignment implemented in the IMOD software package. STEM-tomograms were reconstructed from the aligned tilt-series using TEMBIR method, which provides less missing wedge artifacts and better signal to noise (SNR) ratio compared to those obtained by conventional weighted back projection (WBP) and simultaneous iterative reconstruction technique (SIRT). The reconstructed tomograms were segmented by thresholding and manual inspection. Segmented tomograms were visualized by surface-rendering method and quantified by VGS Avizo software to get inter-particle nearest neighbor distance. Surface rendered tomogram of Au/TiO_2 (high mag.), Au/TiO_2 (low mag.), and $AuIr/TiO_2$ are shown in Figure 2.12, 2.13, and 2.14, respectively. Tomogram movies are also freely available through the ACS Publications website at DOI: 10.1021/acs.nano-lett.5b03585.

Supplementary Figures

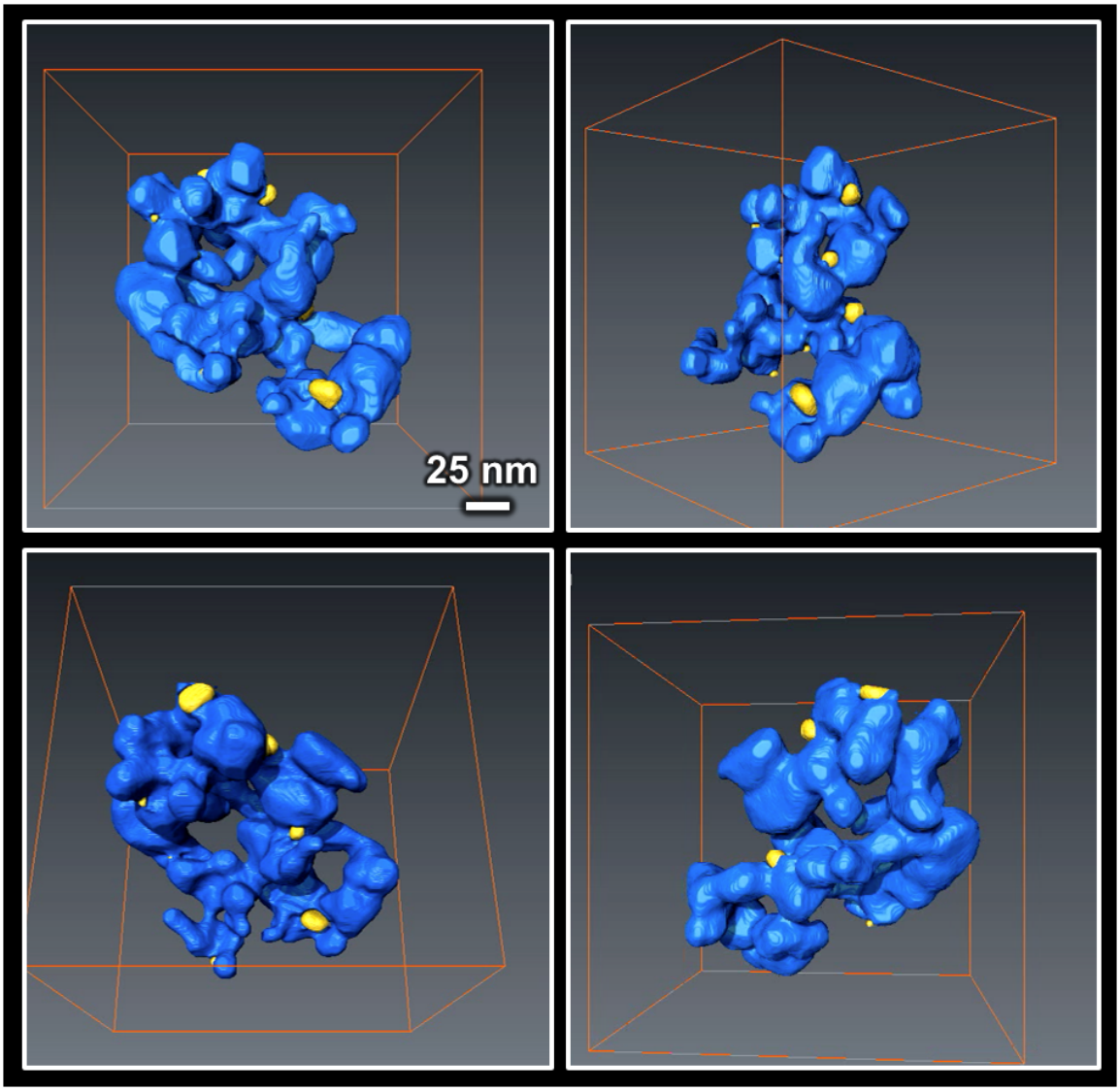

Figure 2.12 Selected frames from the surface rendered tomogram movie of Au/TiO_2 (High mag.).

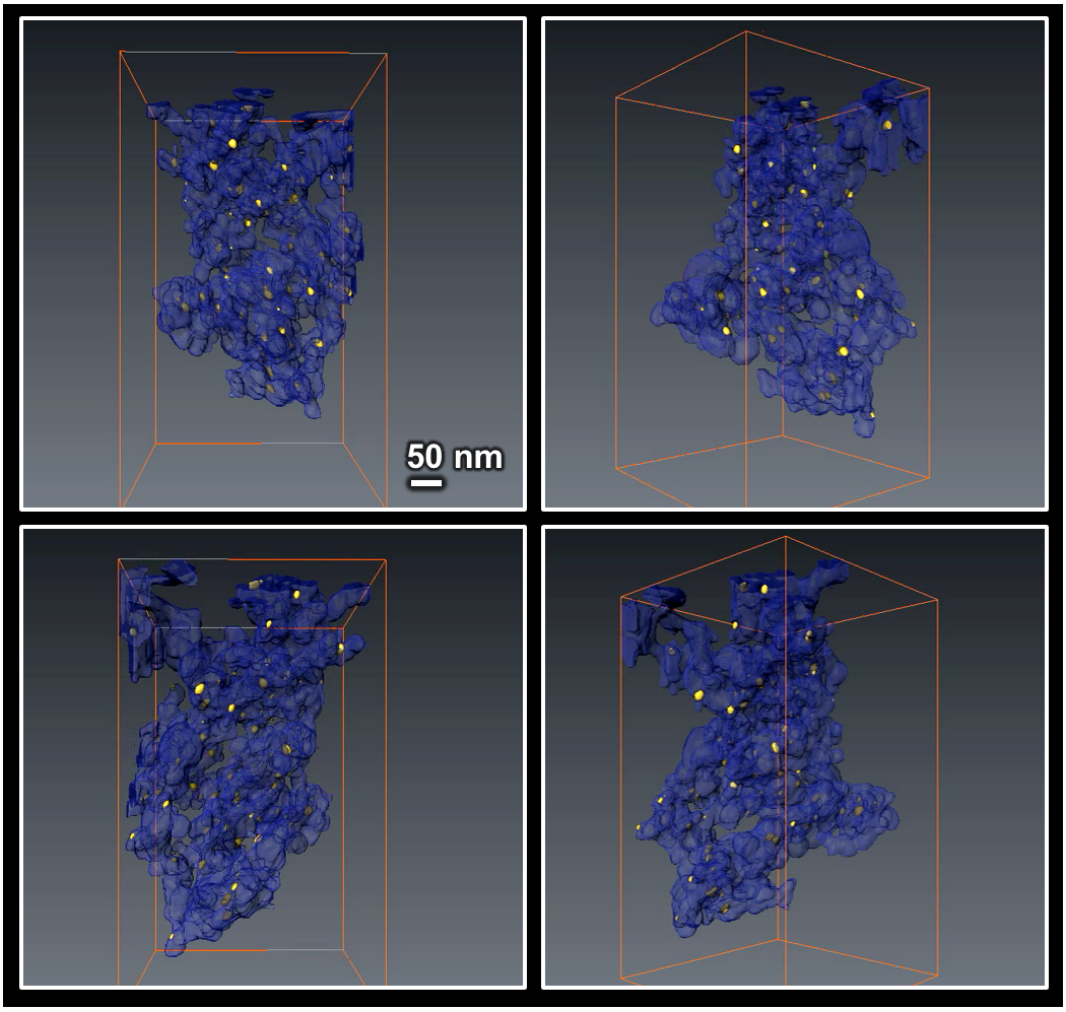

Figure 2.13 Selected frames from the surface rendered tomogram movie of Au/TiO_2 (Low mag.). For better visibility of Au nanoparticles, TiO_2 supports are transparently rendered.

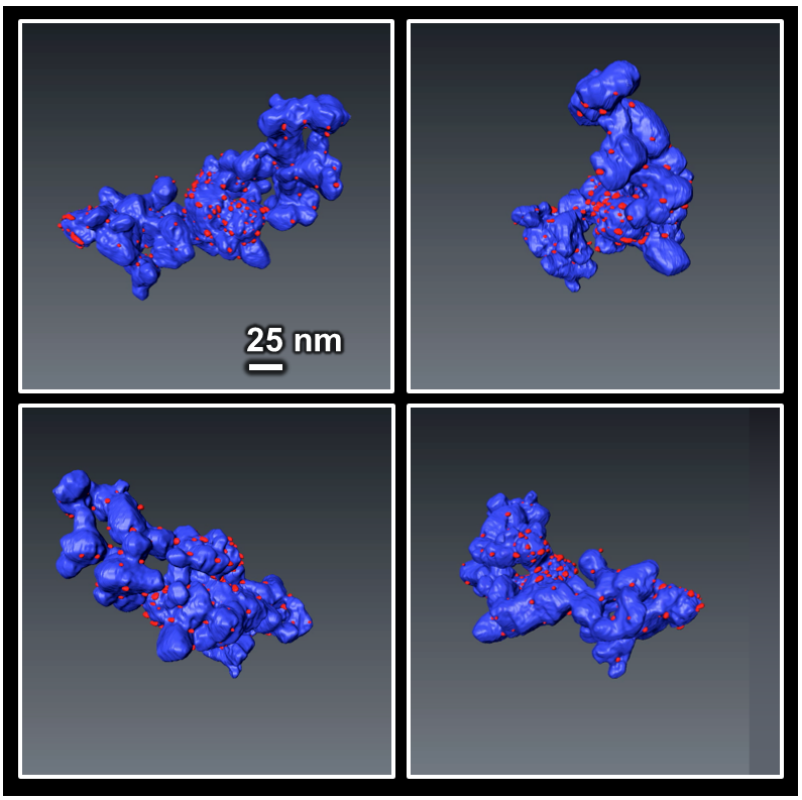

Figure 2.14 Selected frames from the surface rendered tomogram movie of AuIr/TiO_2.

Acknowledgement

This work was supported by the Designing Materials to Revolutionize and Engineer our Future (DMREF) program of the National Science Foundation (CBET-1437219). Aberration-corrected STEM data were partly collected using the FEI Titan S 80-300 TEM/STEM under ORNL's Shared Research Equipment (ShaRE) User, which is sponsored by the Office of Basic Energy Sciences, the U.S. Department of Energy. Computational resources provided by the National Energy Research Scientific Computing Center (NERSC) are gratefully acknowledged. R. Zanella and A. Aguilar-Tapia acknowledge the financial support granted by PAPIIT 103513, UNAM, Mexico.

2.3 Sequential Aberration-Corrected STEM Imaging of Ir/MgO Catalyst: Visualization of Surface Migration

2.3.1 Introduction

Because surface transport is important in the sintering of supported metal catalysts (one of the major causes of catalyst deactivation),[71] there is a strong motivation to find visual evidence of the migrating species, including isolated metal atoms and metal clusters. Understanding of the surface transport and metal aggregation may lead to methods for stabilizing supported metal catalysts as well as to insights into the dynamics of the catalytic species as influenced by their interactions with supports.

Direct visualization of atomic-scale surface diffusion processes is challenging because it requires fast imaging with atomic resolution. Scanning tunneling microscopy (STM) has been widely adopted in the characterization of solid catalysts—because it allows imaging of individual atoms with high sensitivity to surface topology—but the applications of STM for probing surface diffusion in real time have been limited because the typical time to record a single atom-resolved image is on the order of a minute.[72–75]

Alternatively, scanning transmission electron micros-copy (STEM) has been shown to provide real-time visualization of dynamic phenomena in materials such as compound semiconductors[76] and catalysts,[77,78] as well as in biological materials.[79] Because the electromagnetic raster scanning process in STEM is inherently faster than the mechanical movements required for STM, STEM is more readily applicable for probing dynamic phenomena.

With the development of spherical aberration-corrected transmission electron microscopy and apparatus for in situ experiments, it has become possible to perform atomic-scale investigations of dynamic processes, such as morphological variations of nanoparticles in gas environments[80,81] and nucleation and growth of nanoparticles in liquid.[82,83] Especially, sub-Ångstrom-sized electron probes with high probe currents can be formed in STEM, resulting in remarkably high spatial resolution and signal-to-noise ratios.[84] More important, the high signal-to-noise ratios in STEM imaging enable high frame rates—on time scales of the order of a second. Furthermore, sub-Ångstrom spatial resolution and the capability of atomic number (Z)-contrast STEM in quantifying three-dimensional atomic configurations[85] bolster the capabilities of high frame rates open many new possibilities for applying of aberration-corrected STEM to visualize atomic-scale dynamics of supported catalysts, which are typically composed of high-Z metal clusters on low-Z oxide supports. Although there have been investigations of the surface migration of nanoparticles and atoms on a carbon film,[86,87] to the best of our knowledge, surface migration of individual atoms and clusters with nuclearities less than about 10 atoms on industrial oxide supports with atomic spatial resolution and sub-second temporal scales has been lacking.

Herein, we report the use of high-angle annular dark-field (HAADF) Z-contrast imaging in a fast-scan aberration-corrected STEM to directly observe the beam-induced surface migration of an iridium atom (Ir_1) and a tri-iridium cluster (Ir_3) supported on MgO, a widely used support for industrial catalysts.

2.3.2 Methods

Such highly dispersed iridium catalysts are active for a wide range of reactions [88]; they were synthesized precisely by reaction of the precursor $Ir(C_2H_4)_2(acac)$ (acac is acetylacetonate) with high-area MgO powder that had been partially dehydroxylated in O_2 at 973 K, as previously reported; the synthesis has been shown to lead to $Ir(C_2H_4)_2$ groups bonded to MgO.[89] Sequential Z-contrast STEM images showing the beam-induced migration of Ir_1 on MgO(100) and of Ir_3 on MgO(110) were collected with a probe aberration-corrected FEI Titan microscope (operating voltage: 300 kV).

Prior to the surface migration experiments, we performed electron beam showering before Z-contrast STEM imaging to make sure that the ligands on the iridium were removed. As previously reported, electron beam showering (i.e., irradiation) is effective for dissociating organometallic molecules (especially, metal–ligand bond cleavage).[90,91] The electron stimulated de-composition processes of organometallic molecules has been demonstrated with $Au(CH_3)_2(acac)$[92,93] and $C_5H_4CH_3Pt(CH_3)_3$.[94,95] In this regard, it is realistic to infer that the iridium atoms in the samples we imaged were ligand-free.

To complement the observations, a series of ab-initio calculations using density functional theory (DFT) was performed with the Vienna ab-initio Simulations Pack-age (VASP)[60,96] to determine adsorption energies and diffusion migration barriers of Ir_1 and Ir_3 on MgO surfaces. In the DFT calculations, the Perdew-Wang exchange-correlation[97] and the projector augmented wave (PAW)[98] method with an energy cutoff of 400 eV were used for the ligand-free iridium. The atomic positions were relaxed until the Hellmann-Feynman forces were less than 4×10^{-3} eV/Å. Brillouin zone integrations during the structural optimization are based on a (3 x 3 x 1) grid of Monkhorst-Pack points.[99] All the calculations were spin unrestricted. Further details of the calculations are given in the section 2.3.5 Supplementary Information.

2.3.3 Results and Discussion

Figure 2.15a shows sequential Z-contrast STEM images of Ir_1 on MgO(100)—the most common and stable MgO surface—with an acquisition time of ~ 0.1 s per frame. The atomic columns of MgO and Ir_1 are clearly resolved. As a consequence of the nature of Z-contrast imaging, the atomic columns of MgO appear darker than the column at which Ir_1 is located. During the sequential acquisition at the chosen scan rate, Ir_1 was observed to be predominantly located on top of the atomic columns (Mg or O sites) in the collected images rather than in hollow (H) sites, verifying that the H sites are energetically less favorable for Ir_1. Consequently, we infer that the time that Ir_1 spends in the H sites is much shorter than the time it spends on top of the columns. However, the adsorption sites of Ir_1 on these sites on MgO(100) cannot be distinguished from each other in a Z-contrast image, because when MgO is viewed along the [100] direction, as

illustrated in Figure 2.15b, each atomic column consists of alternating Mg and O (i.e., Mg-O-Mg-O… or O-Mg-O-Mg…). Therefore, the average integrated intensities of the atomic columns in the images are indistinguishable. Although the exact site of Ir_1 is not directly determined by the data, evidence provided by extended X-ray absorption fine structure (EXAFS) spectroscopy indicates that the Ir atoms in the ligated complexes $Ir(C_2H_4)_2$ are bonded to two O atoms each.[80,82] A key observation from the sequential STEM images is that Ir_1 mainly prefers to hop diagonally back and forth across the H sites. This observation reveals that Ir_1 has a tendency to be preferentially adsorbed on particular surface sites.

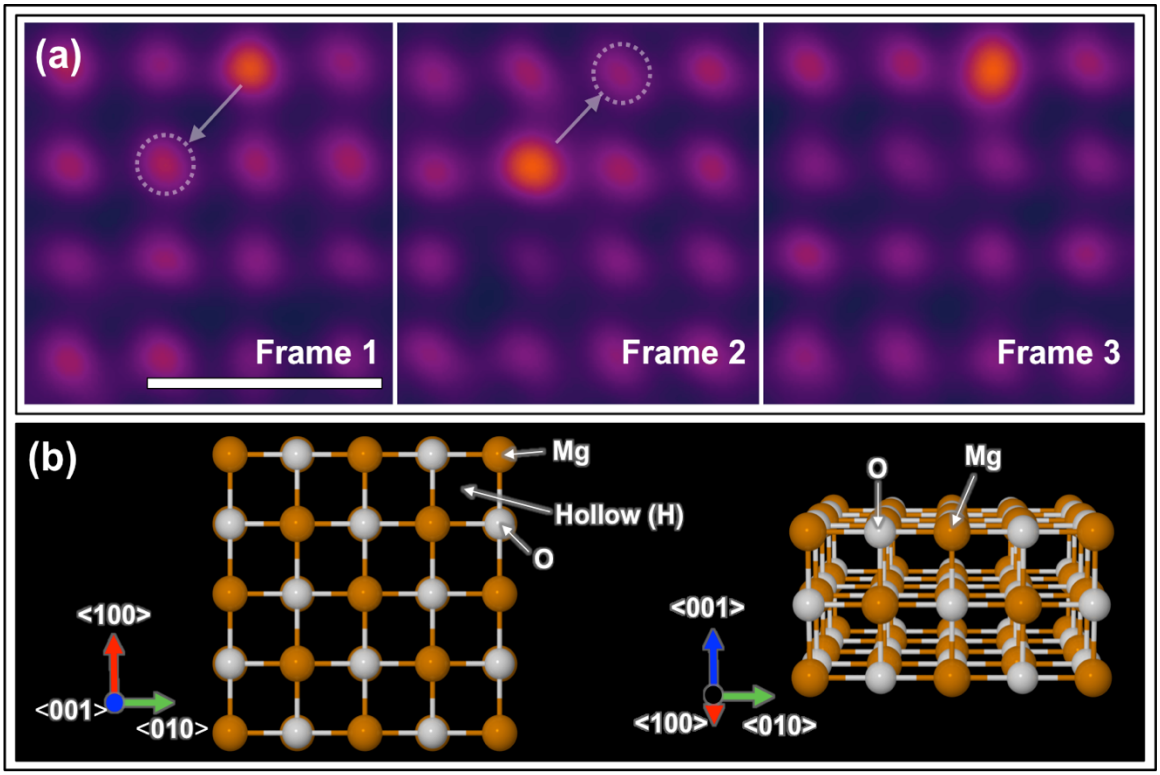

Figure 2.15 (a) Sequential Z-contrast STEM images showing diagonal jumps of Ir_1 on MgO(100). (b) Atomic configurations of a MgO(100) slab. (Scale bar: 5 Å)

To understand the diagonal jumps and the preferential adsorption of Ir_1 on MgO(100), we performed DFT calculations to determine the relative binding energy (RBE) with respect to the most stable configuration, with the binding energy (BE) defined as follows:

$$BE = \frac{E_{MgO+Ir_x} - E_{MgO} - xE_{Ir_{1,is}}}{x} \quad \ldots (1)$$

where $E_{MgO+Irx}$, E_{MgO}, and $E_{Ir1,is}$ are total energies of the MgO support with an adsorbed Ir_x species and without an adsorbed Ir_x species, and an isolated Ir atom, respectively (x is the number of Ir atoms (x = 1 corresponds to an mononuclear iridium species; x > 1 corresponds to an iridium cluster).

We found that the site preference for Ir_1 binding on the MgO(100) surface is O followed by H, and then Mg, with the corresponding RBE values of 0, 0.70, and 1.60 eV/Ir atom, respectively. This comparison suggests that the preferential adsorption site of an Ir_1 is the O site and the migration of an Ir_1 on MgO(100) surface would occur between the O sites across the H site. These theoretical results show consistency with our experimental observation that Ir_1 jumps diagonally across the MgO(100) surface; the interpretation is consistent with the inference based on EXAFS spectroscopy [100] that O sites are ligands of the iridium.

Figure 2.16a shows sequential Z-contrast STEM images representing the migration of an Ir_3 cluster on MgO(110), which is not only chemically reactive[101] but also provides an excellent opportunity for determining the adsorption sites of supported metal clusters. When the MgO support is tilted along the [110] zone axis, as illustrated in

Figure 2.16b, each atomic column contains a single kind of atom (Mg-Mg-Mg… and O-O-O…) and, therefore, Mg sites and O sites of the surface are distinguishable in terms of the intensities in the Z-contrast images. However, the sites at valleys (Mg(V) and O(V)) and peaks (Mg(P) and O(P)), illustrated in Figure 2.16b are not readily differentiated in such images. In the sequential images, Ir_3 (highlighted with the yellow square in Figure 2.16a) migrates towards a larger iridium cluster in a step that illustrates the sintering process.

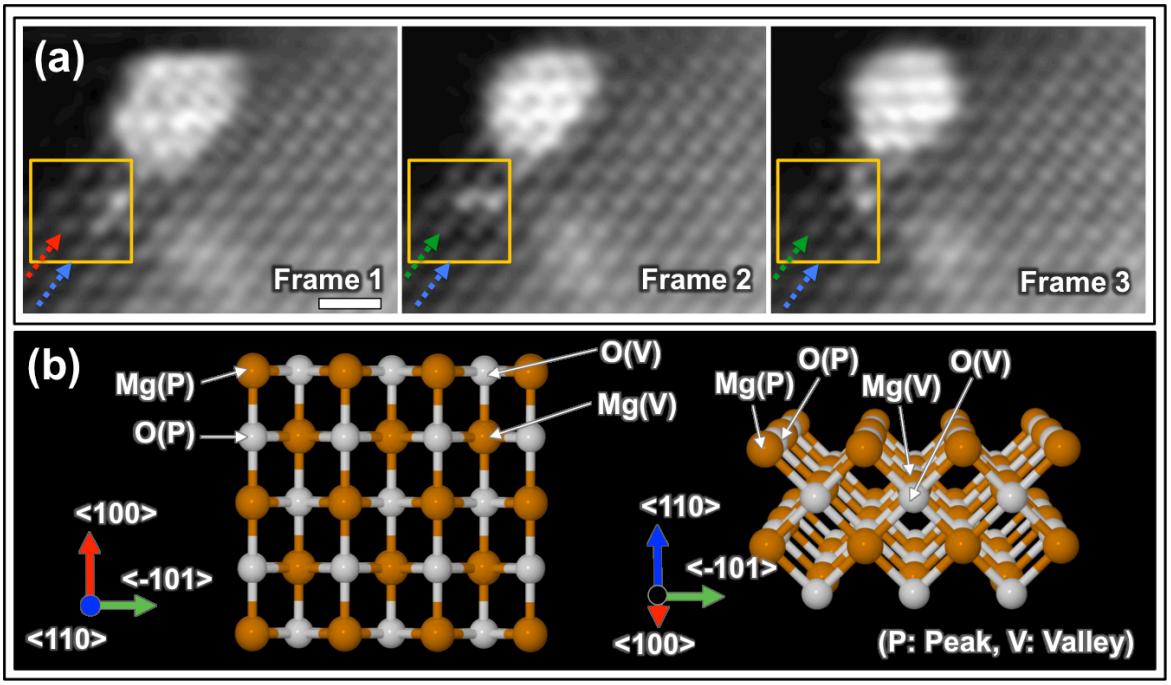

Figure 2.16 (a) Sequential Z-contrast STEM images showing rotational migration of Ir_3 on MgO(110). (b) Atomic configurations of MgO(110). (Scale bar: 5 Å)

By comparing the measured intensity profiles of Ir_3 (along the directions of the blue and the green arrow shown in Figure 2.16a) with the reference intensity profile of

MgO measured along the direction of the red arrow (frame 1 in Figure 2.16a), the nuclearity of Ir_3 and the locations of Ir atoms comprising it have been determined (Figure 2.17a). We found that the Ir atoms in the Ir_3 cluster are adsorbed only on the Mg(V) sites, on which an Ir atom can be bonded to two O(P) sites. Two Ir atoms (Ir_2, arrow in Figure 2.17a) are stacked upright on an Mg(V) site (i.e., the Ir–Ir bond axis is nearly parallel to an Mg column), and the third Ir atom (Ir_1) rotates (in our case in a clockwise direction) around the stacked Ir atoms through the other Mg(V) sites.

Thus, the imaging of Ir_3 on MgO(110) determines the migration mechanism of Ir_3, involving the rotation of one Ir atom around the other two Ir atoms stacked upright on a Mg(V) site and bonded with two O(P) sites. Figure 2.17b illustrates this rotational migration mechanism of the Ir_3 cluster observed in sequential STEM images.

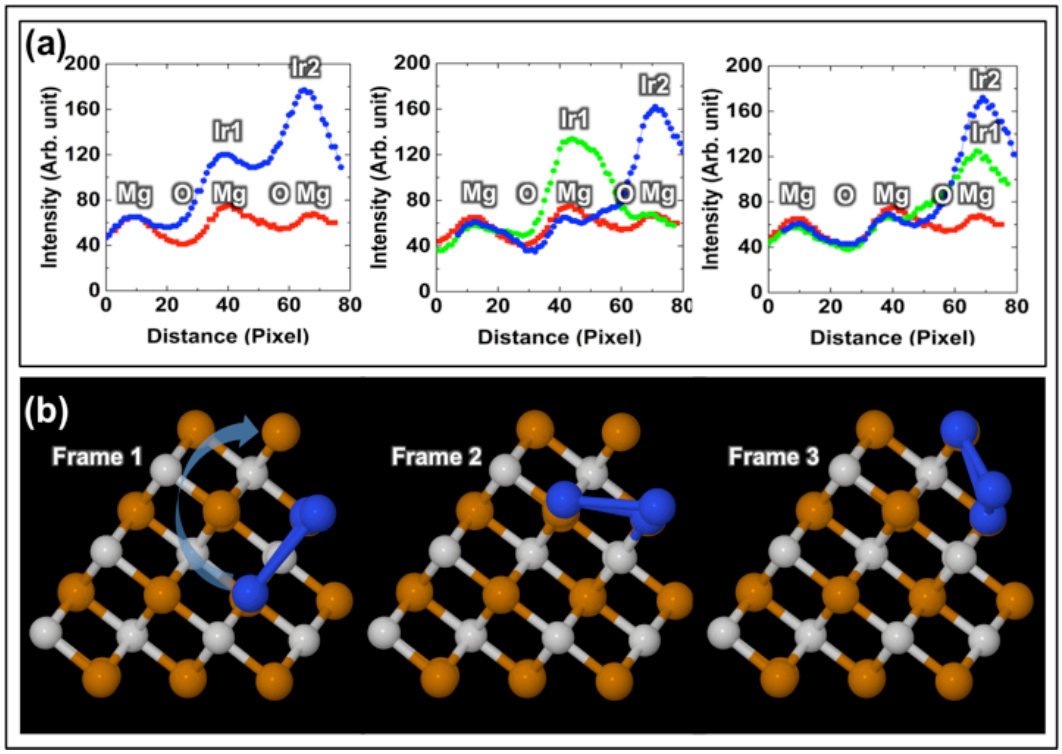

Figure 2.17 (a) Intensity profiles measured from the sequential STEM images (b) Atomic models illustrating the rotational migration mechanism of Ir_3 on the MgO surface.

Although we have directly visualized the migration process of an Ir_3 cluster on MgO(110) using aberration-corrected STEM, these images are not sufficient to determine the adsorption energies and rate-determining parameters, such as the migration barrier of Ir_3 on MgO. Thus, we performed DFT calculations, which showed six different energetically favorable configurations in the order of the increasing RBE values, shown in Figure 2.18. Most of the configurations (defined in the caption of Figure 2.18) except C6 are more stable than C5 (an in-plane triangular arrangement of Ir_3), and, therefore, it is expected that the frequency of observation for these configurations during STEM imaging will be higher than that of the in-plane geometry of Ir_3.

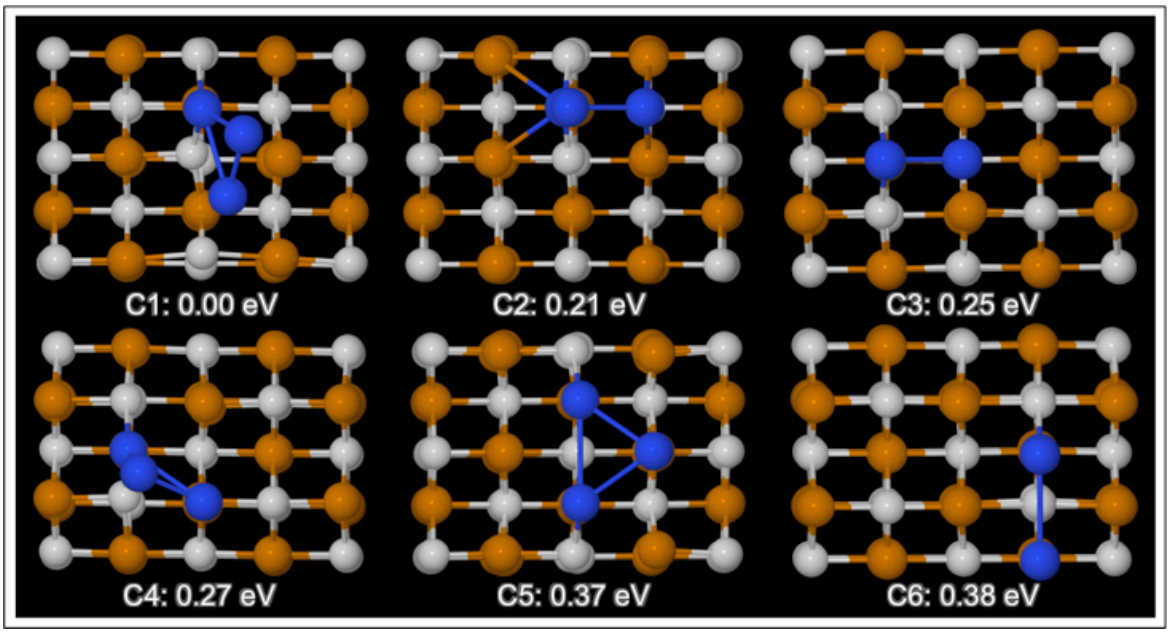

Figure 2.18 Energetically favorable configurations of Ir_3 on MgO(110) surface in order of the relative binding energy.

We stress the comparison between the experimentally observed atomic configurations of Ir_3 and the energetically favorable configurations predicted by the DFT calculations. From the theoretical point of view, we expect the C1 configuration to be the most frequently observed one during the experiment, because C1 is energetically more favorable than any other configuration. However, the experimental observation shown in the first frame of the sequential STEM images (Figure 2.19a) is not consistent with the asymmetric C1 structure (Figure 2.19b) but more like the symmetric C6 configuration (Figure 2.19c), which is less stable by as much as 0.38 eV.

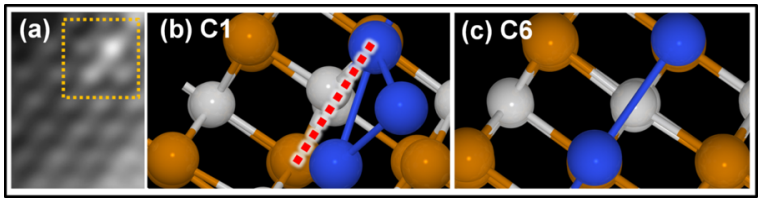

Figure 2.19 Direct comparison of experimentally observed configurations (a) with theoretically predicted configurations C1 (b) and C6 (c).

This point can be understood by the time averaging effect in the experiment. When comparing the theoretical configuration (here, C1, Figure 2.19b) with the experimental observation (Figure 2.19a), we need to consider the mirror configuration of C1 (C1'), which can be generated by mirroring C1 along the dotted line in Figure 2.19. Because the energy of C1' will be the same as that of C1, the flipping between C1 and C1' can take place at a very high frequency, much faster than the experimental temporal resolution. The averaging effect leads to the observation of an asymmetric C1 configuration as the symmetric one (i.e., C6, Figure 2.19c), and this effect has also been known for Si dimers of Si(100).[102] In this sense, time averaging should also be taken into account when the theoretical configurations are directly compared with the experimental observations.

However, the energetically favorable configurations demonstrated by the DFT calculations are generally consistent with the experimentally observed ones in which two Ir atoms are vertically stacked on an Mg site. Specifically, theoretically predicted configurations show that the two Ir atoms stacked on top of each other (hereafter, Ir_{2s}) are preferentially located on top of the Mg(V) site, where Ir_{2s} can be bonded to two O(P) sites, as previously described.

Besides determining the stable configurations and corresponding RBE values, we used the nudged elastic band (NEB) approach[103] to calculate the energy barrier of the rotational migration of Ir_3 following the frames shown in Figure 2.3.3b, finding an energy barrier of 0.44 eV.

2.3.4 Conclusions

In summary, we have visualized the surface migration of an Ir1 atom on MgO(100) and of an Ir_3 cluster on MgO(110) by sequentially collecting Z-contrast images using fast-scan aberration-corrected STEM. The sub-second temporal resolution and the atomic spatial resolution allowed capture of individual atomic scale steps in the surface migration of Ir_1 and Ir_3 on MgO surfaces. Theoretical DFT calculations confirm the experimental observations and provide more detailed quantitative information characterizing the fundamentals of the observed surface migration (migration energy barriers and binding energies). Thus, the combination of fast-scan aberration-corrected STEM and DFT calculations has determined the migration mechanisms of Ir_1 and Ir_3 on MgO: Ir_1 is preferentially adsorbed on the O sites and jumps from O site to O site on MgO(100). Ir_3 on MgO(110) migrates through the rotational mechanism of the Ir_1 around Ir_{2s} located on the Mg(V) site. These results demonstrate that fast-scan aberration-corrected STEM combined with DFT is powerful for investigating the surface transport mechanisms of supported metal species and for understanding of catalyst sintering and deactivation.

2.3.5 Supplementary Information

Materials and Methods

Materials and Sample Synthesis

The MgO support was obtained from EM Science. A paste was obtained by adding deionized water to the MgO, and dried overnight in air at 120 ºC. The resultant solid was ground and treated in flowing O_2 as the temperature was ramped linearly at a heating rate of 3 °C/min from room temperature to 700 °C and then held for 2 h in O_2 flow following by evacuation for 14 h at 700 °C, resulting in a high degree of dihydroxylation. The resultant calcined MgO was then cooled to room temperature under vacuum and transferred to an argon-filled glove box (< 1 ppm O_2 and < 1 ppm H_2O). The surface area of final calcined MgO is approximately 100 m^2/g. The precursor, $Ir(C_2H_4)_2(acac)$, was synthesized as described before, and stored in an argon-filled glove box. To prepare the supported catalyst containing 1.0 wt% Ir, 54 mg of $Ir(C_2H_4)_2(acac)$ and 2.946 g of calcined MgO were slurried in dried and deoxygenated *n*-pentane (Fisher, HPLC grade, dried and purified by a Grubbs apparatus, MBraun SPS, in the presence of argon) that was initially at dry-ice temperature. The slurry was mixed for two days at dry-ice temperature, and thereafter the solvent was removed by evacuation for a day. The resultant supported iridium sample was light gray in color. It was stored in an argon-filled glove box.

Sample Handling

To transfer the supported iridium sample to the TEM facility, it was first packed in small vials and wrapped with paraffin film under argon atmosphere. Then, the vials were placed in a 10-cm vacuum tube sealed with vacuum flanges from both sides. The sealed vacuum tube was then shipped to the TEM facility. At the TEM facility, the sealed vacuum tube containing the samples were transferred into a glove bag filled with ultrahigh-purity argon. In there, the tube was opened and the samples were loaded into a lacey carbon grid, which was inserted in a TEM holder under argon. The glove bag was next moved to the microscope and briefly opened, whereupon the TEM holder was transferred quickly to the microscope. The turbo-molecular pump used to evacuate the microscope chamber was switched on several minutes before insertion of the sample to allow the attainment of its operational speed. The pumping on the airlock was begun immediately after the specimen was inserted into the microscope. We estimate that the time period during which trace contaminants of air might have intruded into the sample holder prior to its insertion into the airlock and re-establishment of the vacuum was less than 5 s.

Experimental

The fast-scan high-angle annular dark-field (HAADF) STEM imaging experiments were performed at 300 kV using an FEI TitanS 80-300 electron microscope at the Center for Nanophase Materials Sciences, Oak Ridge National Laboratory. This microscope was equipped with a high brightness XFEG field emission gun and a CEOS dodecapole probe (STEM) aberration corrector. The images were captured by a HAADF detector with a

probe convergence angle of 27.5 mrad and with collection angle from 50 to 200 mrad. Intensities of atomic columns in the sequential Z-contrast images were quantified using the ImageJ software.

Density Functional Theory Calculation

To investigate the relative stability of the different adsorption configurations of Ir(1-3) clusters on both (110) and (100) MgO surfaces, calculations were performed using Density Functional Theory (DFT) as implemented in the Vienna *ab-initio* Simulations Package VASP with Perdew-Wang exchange-correlation functionals. We have used the projector augmented wave (PAW) potentials with cutoff of 400 eV. The atomic positions were relaxed until the Hellmann-Feynman forces were less than $4x10^{-3}$ eV/Å. Brillouin zone integrations during the structural optimization are based on a (3x3x1) grid of Monkhorst-Pack points. MgO (110) surfaces were modeled using periodic symmetric seven-layer slabs, and a vacuum region of 19.16 Å, while MgO (100) were modeled using asymmetric four-layer slabs and a vacuum region of 11.26 Å. The middle/bottom layers were fixed at the calculated bulk lattice constant 4.207 Å, in the case of symmetric/asymmetric slabs, respectively. The calculated lattice constant is in agreement with previous *ab-initio* pseudopotential calculations (4.16 Å) and experimental measurements (4.207 Å at 19.8 K).

The extent of the vacuum region was chosen larger for the (110) surface to accommodate the Ir_3 clusters adsorbed on both faces of the slabs, to ensure minimum interaction

between the images. We used (2ax2a) and (2ax2a$\sqrt{2}$) surface cells to describe the (100) and (110) surfaces, respectively, where a is the lattice parameter.

Acknowledgement

This research was supported by ORNL's Shared Research Equipment (ShaRE) User Program, which is sponsored by the U.S. Department of Energy (DOE) Office of Science, Basic Energy Sciences (BES); computer time at the Fusion computer facility, Carbon cluster at the Nanoscience and Technology center at Argonne National Laboratory under contract DE-AC02-06CH11357; and in part by the Chemical Imaging LDRD Initiative at Pacific Northwest National Laboratory, which is operated by Battelle Memorial Institute for the U.S. Department of Energy under Contract No. DE-AC05-76RL01830. Work at the University of California was supported by DOE BES grant FG02-04ER15513.

2.4 *In-situ* TEM Study of a Thermal Behavior of Au-Fe_3O_4 dumbbell-like nanoparticles: Discovery of Strong Metal-Support Bonding of Gold on Iron Oxide

2.4.1 Introduction

Metal nanoparticles (NPs) supported on an oxide support have been one of the most important types of heterogeneous catalysts for producing chemical products as well as for exhaust gas clean-up. It has long been known that the catalytic performances including the activity, selectivity, and stability are strongly dependent both on the supported metal NPs itself and on the metal support interaction. Since the metal support interaction can dramatically change the catalytic property and the stability, many efforts have been made to understand and utilize the interaction for the real catalytic applications.

Among the parameters determining the catalytic properties, the strength of the metal-support bonding (MSB) is of utmost importance for the industrial heterogeneous catalysts because MSB directly determines the stability (i.e., lifetime) of the supported catalytic metal NPs.[104] This is especially critical for the supported gold catalysts owing to their low sintering resistance. Since the discovery of the high catalytic activity of gold NP catalysts for low temperature CO oxidation,[28,29] gold catalysts have been significantly studied for various chemical processes for which they showed excellent catalytic activities.[105] Despite the high potential of the gold catalysts for greener chemical processes, the rapid deactivation of them by the sintering of the gold NPs limits the realization of a wide range of industrial applications of the supported gold catalysts.[35,37]

Over the past two decades, numerous studies on the MSB between gold and metal oxide supports have been conducted. Among various metal oxides, CeO_2 has attracted significant attention because Au/CeO_2 shows not only high catalytic activities[106–108] but also highly stability against sintering.[109] It has been found that the strong MSB (SMSB) of gold with surface oxygen vacancies on CeO_2 is the origin of the high stability of Au on CeO_2.[109] More importantly, the metal-support interaction was highly dependent on the morphology/surface structures (facets)[109,110] and the size[111] of CeO_2 support particles. This emphasizes the importance of the precise control of the metal oxide supports in rational design of a stable gold catalyst. In spite of its significance, there has been no study reported on the size-dependency of the SMSB of iron oxide.

Here, we report *in-situ* transmission electron microscopy (TEM) results showing a direct experimental evidence of the SMSB between gold and iron oxide in the Au-Fe_3O_4 dumbbell nanoparticles (DNPs), where the average diameters of the Au NPs and the Fe_3O_4 NPs are 5.0 nm and 10.4 nm, respectively. Drastic morphological changes of Au NP from a spherical NP to a few atomic layer Au film (i.e., complete wetting) on Fe_3O_4 during the vacuum annealing directly indicates the presence of SMSB between Au and Fe_3O_4 during the *in-situ* annealing experiment. To the best of our knowledge, this is the first discovery of the SMSB of gold - iron oxide system.

2.4.2 Methods

Materials and Chemicals

The following chemicals were purchased and used as-received without further purification: anhydrous ethanol (C_2H_5OH, 200 proof, ACS/USP grade, Pharmco-Aaper), hexanes (C_6H_{14}, technical grade, naphtha solvent, Fisher), isopropanol (C_3H_8O, certified ACS plus, Fisher), gold(III) chloride trihydrate ($HAuCl_4$-$3H_2O$, $\geq$ 99.9% trace metals basis, Aldrich), iron(0) pentacarbonyl ($Fe(CO)_5$, Aldrich), borane tert-butylamine complex (BTB, $C_4H_{14}BN$, 97%, Aldrich), 1-octadecene ($C_{18}H_{36}$, technical grade, 90%, Alfa Aesar), oleic acid ($C_{18}H_{34}O_2$, technical grade, 90%, Aldrich), and oleylamine ($C_{18}H_{33}NH_2$, $\geq$ 98% primary amine, Aldrich).

Organometallic Synthesis

Bifunctional composite Au-Fe_3O_4 dumbbell-like nanoparticles (DNPs) were prepared by initiating the epitaxial growth of Fe on Au nanoparticle seeds[112] followed by Fe oxidation in an organometallic solution synthesis.[113–115] Organic methods of synthesis were employed to tightly regulate the size distribution of the nanoparticles and to direct the controlled growth of Fe_3O_4 on the exposed (111) facets of the Au seeds.

Synthesis of Au Nanoparticles

Au nanoparticle seeds were prepared by mixing 0.1 mmol of $HAuCl_4$-$3H_2O$ in 10 mL of oleylamine and 10 mL of hexanes. The solution was heated to 40°C and purged under inert Ar gas. After 10 min, 0.2 mmol of borane tert-butylamine complex (BTB) dissolved

in 1 mL of oleylamine and 1 mL of hexanes was quickly injected and the solution was stirred for an additional 1 hr as the nucleation and growth of the nanoparticles proceeded. The Au nanoparticles were washed with ethanol and re-dispersed in hexanes for further use.

Synthesis of Au-Fe_3O_4 Nanoparticles

To synthesize Au-Fe_3O_4 nanoparticles, 0.5 mL of oleic acid was added to 20 mL of 1-octadecene. The solution was stirred and purged with Ar gas at 120°C for 15 min. 0.02 mL of $Fe(CO)_5$ in 1 mL of 1-octadecene was injected into the solution. The solution was stirred at 120°C for 20 min. 0.5 mL of oleylamine added to 10 mg of Au seeds dispersed in 2 mL of hexanes. This seed solution was quickly injected into the reaction mixture. The resulting solution was rapidly heated to 300°C and held at refluxing conditions for 15 min. The resulting Au-Fe_3O_4 dumbbell-like heterodimers were cooled to room temperature and washed with isopropanol to remove excess surfactants.

In-situ high temperature TEM imaging

In-situ TEM videos (2024*2024 resolution) were collected at 300 kV using a probe aberration-corrected FEI Titan-S 80-300 equipped with a Gatan OneView CMOS camera and a Protochips Aduro MEMS heating stage at Oak Ridge National Laboratory. Thanks to a low thermal-drift rate of the MEMS heating stage during the annealing, morphological transformations of the DNPs could be investigated from room temperature to 550 °C at the same locations and same particles. The electron beam-current and the

dose rate were 3.32 nA and 87300 e/nm^2-sec, respectively. The frame rate of collecting the videos were variably chosen from 10 fps to 25 fps. Due to the huge size of videos (a few TB in total, ~ 6 MB/frame), only the first frame of each minute could be chosen and aligned using the StackReg code[116] implemented in the ImageJ[117] to make a drift corrected *in-situ* video shown in Figure 2.4.1. Therefore, although raw videos have a higher frame rate (i.e., 10 fps to 25 fps), the final corrected videos have a frame rate of 1 fpm. We repeated *in situ* TEM experiments at a lower acceleration voltage, 60 kV to make sure the wetting process was not induced by an energetic electron beam (300 kV). The beam-current and the dose rate for the 60 kV experiments were 3.26 nA and 57200 e/nm^2-sec.

In-situ STEM-EELS

In-situ STEM-EELS were performed at 500 °C on a 300 kV FEI Titan ETEM 80-300 equipped with a Gatan Tridiem GIF with an energy dispersion of 0.3 eV/ch and Gatan single tilt 752 heating stage. The STEM probe current (Spot size 4) was 0.078 nA (dose rate: 87.7 e/Å^2-sec) and the camera length was 100 mm to increase the collection efficiency, although the signal to noise ratio of ADF-STEM imaging was not the optimal. The GIF entrance aperture was 2 mm and the acquisition time per spectra was 2 seconds with a vertical binning of 8.

ADF-STEM Tomography

3D structures of the pristine DNPs were analyzed by ADF-STEM electron tomography. An ADF tilt series (1024*1024 resolution, 5 second frame time) was collected from -70 ° to 52 ° with 2 ° increment. The magnification during the tilt series collection was 450 kX and the probe current was 0.296 nA (spot size 6). The tilt series was aligned by the fiducial marker alignment using the IMOD software[25] and the aligned tilt series was reconstructed using a model based iterative algorithm implemented in the TEMBIR software.[19] 3D visualization (volume rendering) of the reconstructed tomogram was performed using the Tomviz software.[118]

X-ray Photoelectron Spectroscopy

XPS data were obtained using a Kratos Axis Ultra DLD spectrometer with monochromic Al Kα radiation (1486.6 eV) at pass energy of 20 and 160 eV for high-resolution and survey spectra, respectively. A commercial Kratos charge neutralizer was used to avoid non-homogeneous electric charge of non-conducting powder and to achieve better resolution. The resolution measured as full width at half maximum of the curve fitted C 1s peak was approximately 1 eV. Binding energy (BE) values refer to the Fermi edge and the energy scale was calibrated using Au 4f7/2 at 84.0 eV and Cu 2p3/2 at 932.67 eV. XPS data were analyzed with CasaXPS software version 2313 Dev64 (www.casaxps.com). Prior to data analysis, the C-C component of the C 1s peak was set to a binding energy of 284.8 eV to correct for charge on each sample. Curve-fitting was performed following a linear or Shirley background subtraction

using Gaussian/Lorentzian peak shapes. The atomic concentrations of the elements in the near-surface region were estimated taking into account the corresponding Scofield atomic sensitivity factors and inelastic mean free path (IMFP) of photoelectrons using standard procedures in the CasaXPS software. Fe_3O_4 nanoparticles and Au/Fe_3O_4 heterodimers were drop cast on silicon wafers attached to a copper sample holder. Bulk Fe_3O_4 powder (<5 μm, 95%) was purchased from Sigma-Aldrich and loaded directly onto a sample holder. In-situ heating was performed using a built in resistive heating block to anneal the samples to 500°C for at least one hour prior to collecting XPS data.

Density Functional Theory calculations

Periodic plane wave Density Functional Theory (DFT) calculations were performed with VASP 5.3.5 using the Projector Augmented Wave Method (PAW) for Fe_2O_3 (0001), Fe_3O_4 (111), FeO (100), FeO (111) and Fe (110) surfaces. Au nanoparticles are represented as Au (111) films in the DFT models, with pseudomorphic registry on the iron oxides and a moiré pattern on Fe (110). Geometries of the models are shown in Figure 2.24. The model construction is explained in greater detail in the Supporting Information. Self-consistent electronic energies are calculated using the PBE functional within the Generalized Gradient Approximation (GGA). The PBE+U approach is employed for partially correcting the pathological self-interaction error prevalent in standard GGA functionals like PBE. Electronic cores of Fe, O and Au are represented by PAW PBE pseudopotentials. Further details including kinetic energy cutoffs, k-points based on the Monkhorst Pack scheme, magnetization and the numerical cut offs

employed for iterative solutions of the Kohn Sham equations are provided in the Supplementary Information. Binding energies of Au films (equation 2), reflecting their heats of adsorption on iron oxide substrates are reported with respect to bulk FCC Au.

2.4.3 Results and Discussion

Figure 2.20 shows snapshots of the *in-situ* TEM movie summarizing the thermal behaviors and morphological changes (i.e., wetting) of the Au-Fe_3O_4 DNPs and Au NPs with increasing temperature. Au NPs were intentionally mixed with the DNPs with the aim of comparing the thermal behaviors of the DNPs and Au NPs (marked with dotted line in Figure 1a). The Au-Fe_3O_4 DNPs were gradually heated up from room temperature up to 550 °C under high vacuum (1.88×10^{-7} Torr) with the heating profile (time vs. temperature) of the *in-situ* TEM experiment presented in Figure 2.20g.

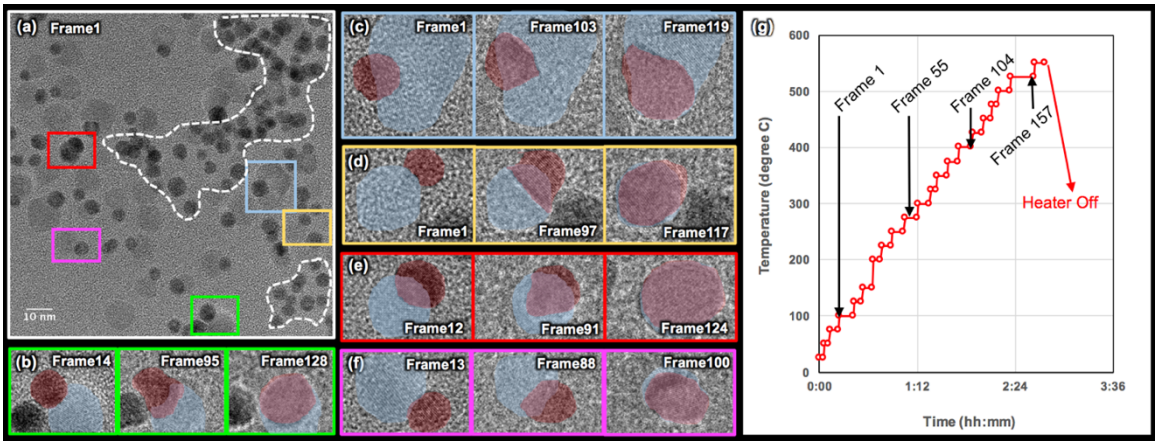

Figure 2.20 Snapshots of an *in-situ* heating TEM movie summarizing the thermal behavior of Au-Fe_3O_4 DNPs. (a) The initial frame taken at ~ 100 °C (b-f) Sequential snapshots showing the wetting behaviors of Au NPs on iron oxide domains. For better visibility, Au and Fe_3O_4 are false colored as transparent red and blue, respectively. (g) Temperature vs. time profile of the annealing experiment.

With increasing the annealing temperature from the room temperature to ~ 350 °C, a neck formation between regular Au NPs (without Fe_3O_4), which is the first step of sintering process, was observed. As the temperature was further increased, the regular Au NPs coalesced together and formed several bigger Au particles. However, the gold domain of the DNPs started to flatten and partially covered the surface of the iron oxide domain at ~ 350 °C (Figure 20.2b-f). As the wetting process further proceed, the iron oxide domain was totally covered by the gold thin film at ~ 500 °C. A thickness of the flattened Au on iron oxide was calculated as 1.9 Å, which corresponds to one monolayer of Au film on an iron oxide NP, assuming the shape of Au and Fe_3O_4 are spherical and their volume are conserved during the entire heating experiment.

The observed structures of one monolayer gold film on a Fe_3O_4 domain indicate that strong bonds (i.e., SMSB) were formed at the interface between Au and Fe_3O_4 during the *in-situ* annealing as much as a metal-substrate (Au-Fe_3O_4) interfacial adhesion is stronger than metal-metal (Au-Au) bonds (or, the surface tension of Au NP). This is surprising, because it is contradictory to the well-known fact that a gold film grown on an extended surface of a single-crystalline Fe_3O_4 substrate at high temperatures (400°C and 750°C) has a 3D island shape rather than a 2D film structure,[119,120] which corresponds to a Volmer-Weber growth mode, wherein the strength of the interfacial adhesion is weaker than gold-gold bonds. The change of the strength of the MSB between the Au-Fe_3O_4 DNPs during the can be estimated by calculating the adhesion energy using Young-Dupré equation (Eq. 1).

$$E_{adh} = \gamma_{np}(1-\cos\theta) \quad \ldots \text{Equation 1.}$$

where γ_{np} and θ is the surface tension of the supported nanoparticle and the contact angle.

In our case of a gold thin film on an iron oxide nanoparticle where theta equals 180 °, the adhesion energy is estimated as 2.56 J/m^2 ($2\times\gamma_{Au(111)}$) and this value is 0.26 J/m^2 higher than the previously reported value of Au(111)/Fe_3O_4(111) (2.3 J/m^2), which reported elsewhere.[121]

The major structural difference between the Au-Fe_3O_4 DNPs and Au/single-crystalline Fe_3O_4 with an extended surface, which might be causing the directly-opposed wetting behavior, is the size and morphology of the nanoFe_3O_4. In our case of the DNPs, the nanoFe_3O_4 domain has only an average diameter of ~ 10 nm. Moreover, due to the large curvature of the nanoFe_3O_4 domain, the chemical potential of the surface atoms on the spherical Fe_3O_4 with ~ 5 nm radius is much higher compared to the extended flat Fe_3O_4, as predicted from the Gibbs-Thomson equation. This higher surface chemical potential possibly causes the surface to be more reactive and form a stronger adhesion with gold than the flat Fe_3O_4 surfaces. According to the report by Carrettin *et al*., Au/nano-CeO_2 (i.e., 3~4 nm CeO_2) has two orders of magnitude of higher catalytic activity for a CO oxidation, compared to Au/regular-CeO_2.[111] The authors claimed that the strong size dependent behavior in the catalytic measurement is due to the large number of oxygen vacancies on the nanoCeO_2 surfaces.

Another remarkable difference between the nanoFe_3O_4 of the DNPs and regular Fe_3O_4 is the facets enclosing the Fe_3O_4 crystal. In contrast to the regular Fe_3O_4, the nanoFe_3O_4 domain in the DNPs are epitaxially grown on the Au NP seeds during the synthesis of the DNPs. Therefore, thermodynamically less favorable Fe_3O_4 (011) and (131) facets[122,123] can be formed along with Fe_3O_4 (111) due to the epitaxial relationship of Au and Fe_3O_4 (Au(220)[112]//Fe_3O_4(440)[112] and Au(111)[112]//Fe_3O_4(222)[112] with a ~2.7 % and ~3 % lattice mismatch, respectively) (Figure 2.21 a, b).

The epitaxial facet developments of Fe_3O_4 in the DNPs were also observed from the annular-dark field (ADF) electron tomography investigation (Figure 2.21 c. d). In this regard, we believe the energetically reactive facets of the DNPs might also contribute to the SMSB.

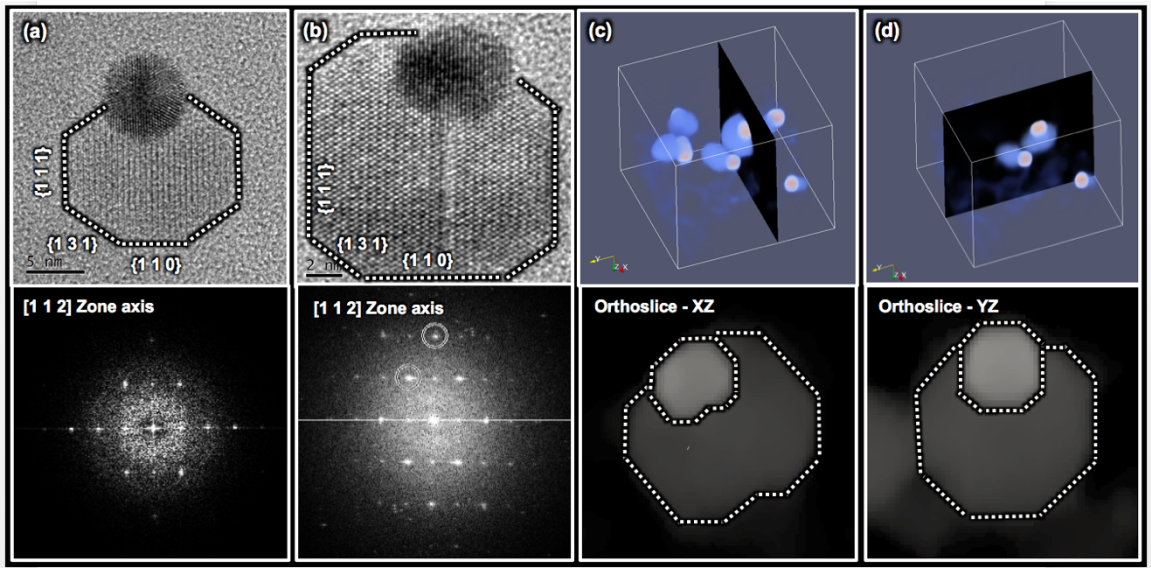

Figure 2.21 HRTEM and 3D Tomogram of Au-Fe_3O_4 showing an epitaxial relationship between Au and Fe_3O_4 (a, b) High resolution TEM images (top) and Fast-Fourier transformation (FFT) patterns (bottom) of Au-Fe_3O_4 DNPs showing the facets of Fe_3O_4. FFT patterns were collected from Fe_3O_4 to determine a zone axis. (c) Volume-rendered ADF-STEM Tomogram (top) and orthogonal slice (bottom) of Au-Fe_3O_4 DNPs showing the facet relationship (Contrast adjustment for the orthogonal slice was performed for a better visibility of Fe_3O_4).

To investigate the changes of the local chemical nature of the DNPs during the vacuum annealing, we performed *in-situ* scanning TEM (STEM) electron energy loss spectroscopy (EELS) during annealing of the Au-Fe_3O_4 DNPs at 500 °C. Several different DNPs, which correspond to the "*initial*", "*intermediate*", and "*final*" state of the gold wetting/flattening process, were characterized. Figure 2.22 shows annular dark-field (ADF) STEM images of the DNP representing one of the above-mentioned states along with the locally collected EEL spectra from the DNPs shown in the STEM images. The locations where EEL spectrum collection was performed and the corresponding spectrum are color-coded accordingly.

The DNP before the flattening maintained its dumbbell shape and a noticeable phase transformation, such as an intermixing between gold and iron oxide, was not observed (Figure 2.22a). However, as can be seen in Figure 2.22b where the hemisphere of iron oxide domain was partially covered by flattened gold, we found that the surface of the "gold covered" iron oxide hemisphere was heavily reduced and consequently, O K edge intensity was negligible. On the contrary, another hemisphere with no Au was remained as a form of an iron oxide, although it was not possible to determine the oxidation state of Fe due to a low signal to noise ratio of the *in-situ* EEL spectra (green spectra in Fig. 2.22b). The final state shown in Fig. 2.22c illustrates that the iron oxide is fully covered by the Au film while the core still remained as an oxide, although the iron oxide surface was highly reduced.

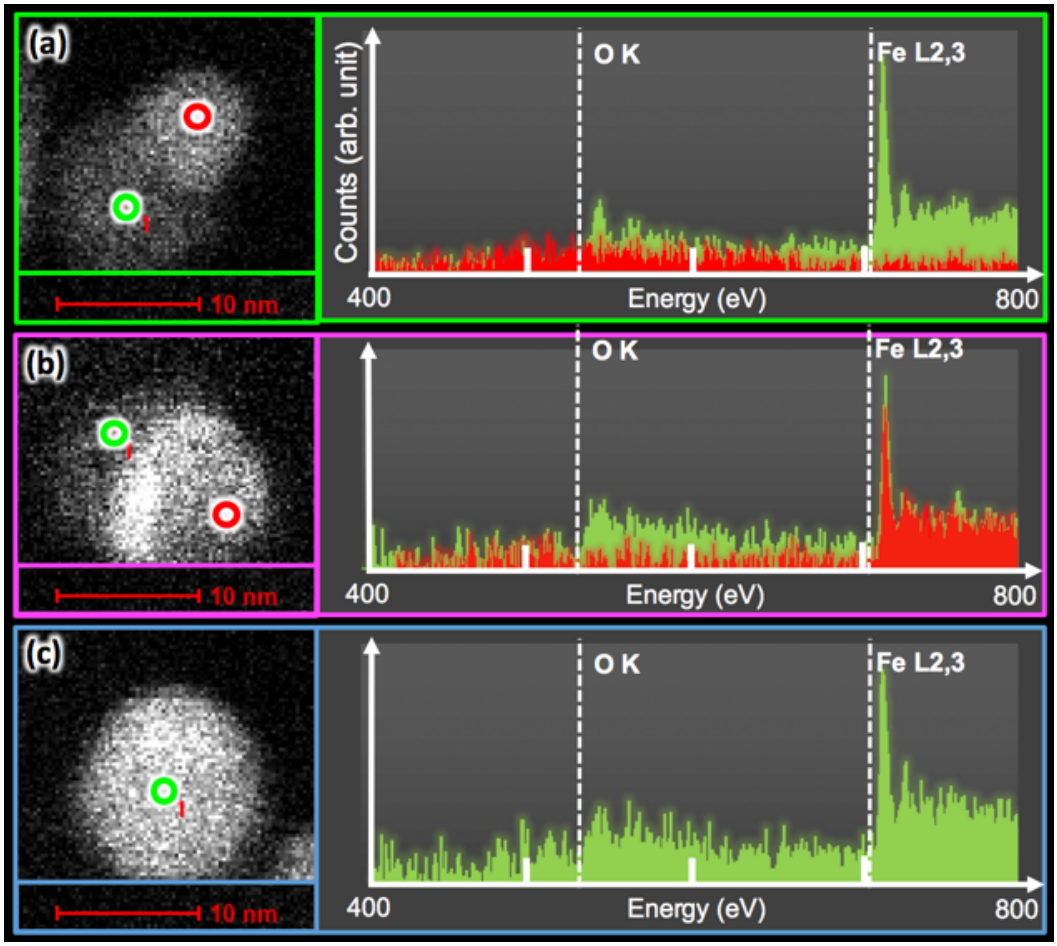

Figure 2.22 Results of *in-situ* STEM-EELS showing ADF-STEM images and EEL spectrum collected from the DNPs at (a) "*initial*", (b) "*intermediate*", and (c) "*final*" state of the wetting/flattening process.

This result suggests that the SMSB in the Au-Fe_3O_4 DNPs is correlated with the surface reduction of the iron oxide domain. The role of surface oxygen vacancies of the metal oxides on MSB has been investigated by several researchers and it has been reported that the surface oxygen vacancies of CeO_2 and TiO_2 strongly adsorb metal atomic species and NPs and stabilize them.[124,125] Moreover, it has also been pointed out that the amount of

surface oxygen vacancies contributing to the strength of MSB is strongly dependent on the facets enclosing the support particles because the redox capability of a metal oxide is dependent on the type of facets.[109,110,126] Therefore, we may conclude that the unique SMSB of the DNPs is due to the higher reducibility (or, higher surface oxygen vacancy concentration) of nanoFe_3O_4 having high surface chemical potential and reactive facets, as discussed above.

In order to determine the oxidation states and progression of the reduction process, we performed X-ray photoelectron spectroscopy (XPS) analysis of the DNPs "before" and "during" vacuum annealing at 500 °C. The heating was performed *in-situ* allowing spectra to be obtained while the sample was held at 500 °C and were given one hour to equilibrate before beginning the acquisition. Before heating the sample to 500 °C, the Fe 2p3/2 main peak is located at 710.5 eV with no distinct shake up feature, which is characteristic[127] of the convolution of the Fe^{3+} and Fe^{2+} features present in Fe_3O_4. During the vacuum annealing, the main Fe 2p3/2 peak shifts to 709.3 eV and a distinct shake up feature appears at 715.6 eV, as shown in Figure 2.23a. Both the peak position and the distance between the main peak and the shake up feature indicate the reduction to Fe^{2+}.[128] Along with the reduction of Fe^{3+} to Fe^{2+}, a prominent feature representing 30% of the total Fe signal appears at 706.8 eV indicating the reduction to metallic iron. Accompanying the reduction of Fe, a shift in the Au 4f7/2 peak from 83.8 eV to 84.2 eV is seen due to the heating, as shown in Figure 2.23b. This 0.4 eV chemical shift can be explained either by a flattening effect or by gold coordinating with iron forming an intermetallic phase.

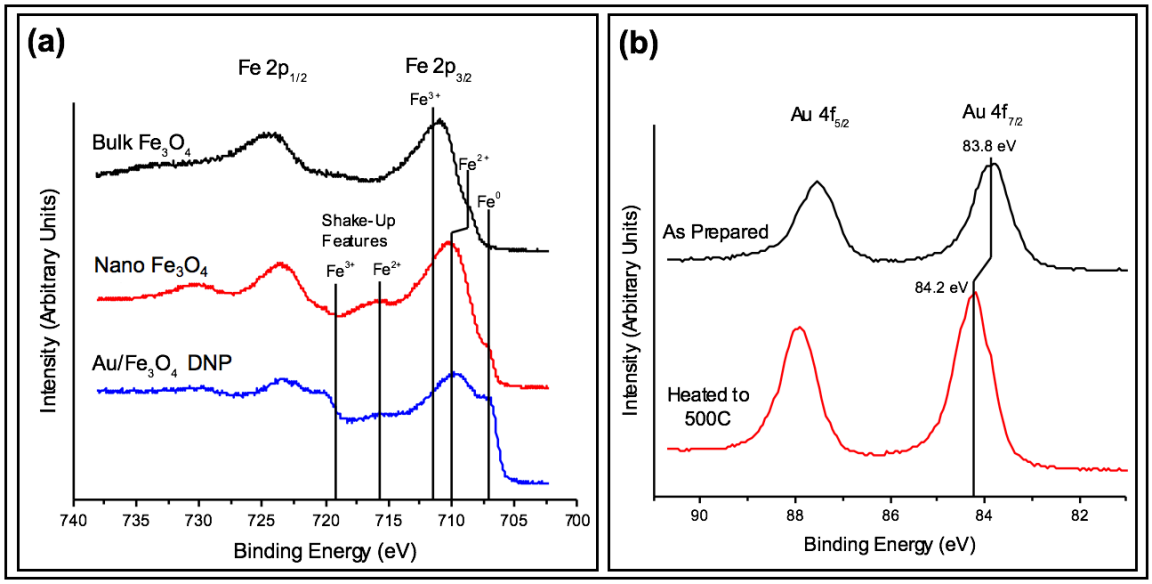

Figure 2.23 (a) F 2p spectra collected at 500 °C for bulk Fe_3O_4, nanoFe_3O_4, and Au/Fe_3O_4 DNPs. Reference lines for the features are shown to help guide the eyes and are taken from Ref[128]. (b) Au 4f spectra from the Au/Fe_3O_4 DNPs taken as prepared and after annealing to 500 °C. (Data was collected and provided by Cory Milligan, Dr. Dmitri Zemlyanov, and Prof. Fabio H Ribeiro)

This XPS result indicating the surface reduction of the nanoFe_3O_4 is interesting. According to Syed *et al.*, a100 nm thick Fe_3O_4 thin film deposited on Si substrate was quite stable against the reduction in the vacuum annealing (from 573 K to 973 K at 9.75×10^{-7} Torr) and therefore, the Fe 2p3/2 peak in the XPS spectra was remained on the same binding energy. Also, a characteristic peak indicating a metallic Fe has never appeared.[129] Similar result was also observed in our *in-situ* XPS measurement of a few micrometer sized bulk Fe_3O_4 at 500 °C in ultrahigh vacuum condition (Figure 2.23a - Blackline). In contrast to the case of nanoFe_3O_4 and Au/Fe_3O_4 DNPs, the Fe 2p3/2 peak of bulk Fe_3O_4 showed a characteristic shape and position of unreduced Fe_3O_4. This

suggests that the spherical nanoFe_3O_4 has a higher reducibility and a higher capability of containing oxygen vacancies on its surface compared to flat extended Fe_3O_4. Furthermore, our STEM-EELS results and this allowed us to come to a conclusion that the SMSB between Au and iron oxide is induced by a unique reducibility of nano Fe_3O_4 of the DNPs.

A similar XPS experiment was performed on the nanoFe_3O_4 NPs synthesized without gold to determine if the reduction behavior is due to the size effect of the nanoFe_3O_4 or if gold plays an important role in the observed reduction phenomena. The spectra, shown in Figure 2.23a - Redline, obtained from "before" and "during" experiments are qualitatively similar to the Au-Fe_3O_4 DNPs. Both show a reduction of Fe_3O_4 to FeO and Fe, but the difference arises in the relative concentration of metallic iron formed. As shown in Figure 2.23a, without the presence of gold only 7.5% of the total iron signal appears as metallic iron compared to the 30% when gold is present. These results prove that the nanoFe_3O_4 is reducible even without gold, although gold accelerates the reduction phenomena. Therefore, the difference in the reducibility between the nanoFe_3O_4 and the extended Fe_3O_4 can be understood as a shape and size-dependent phenomena. Moreover, it can be concluded that the higher concentration of the surface oxygen vacancies on the Fe_3O_4 domain causes the SMSB.

We performed first principles Density Functional Theory (DFT) calculations to investigate the SMSB in the Au-Fe_3O_4 DNPs observed upon reduction of the surface during *in-situ* annealing. The interaction of a progressively reducing iron oxide support

with Au nanoparticles was studied by performing a trend based analysis of the stability of Au (111) films on a range of single crystal iron oxide surfaces, with a variety of oxidation states – starting from the most oxidized (Fe_2O_3), to partially reduced (Fe_3O_4), and finally to the most reduced (metallic Fe) supports. In addition, since XPS clearly shows the presence of Fe^{2+}, we also studied Au binding energies on model FeO surfaces. In reality, FeO seems to be amorphous phase not a crystalline phase based on our *in-situ* electron diffraction experiment, in which no reflections from crystalline FeO phase was observed. Therefore, more accurate description on the phase containing Fe^{2+} might be highly reduced FeOx. Although not stable in the bulk phase, FeO serves as a simple model to simulate the effect of Fe^{2+} on stability of Au films, and allows us to compare trends in Au binding energies with oxidation state of Fe.

We studied Au (111) films with a pseudomorphic registry on Fe_2O_3 (0001), Fe_3O_4 (111) and FeO (111) while a moire pattern of the film on Fe (110) was studied to minimize strain effects. In addition to calculating binding energies, the stability of Au films on Fe_2O_3 (0001), Fe_3O_4 (111), FeO (111) and Fe(110) has been evaluated using an *ab initio* phase diagram approach.

Binding energies ($E^{binding}$) on the oxygen and iron terminated surfaces of various iron oxide models are shown in Figure 4(a). The binding energies were calculated as,

$$E^{binding} = \frac{E_{Au\ on\ FexOy} - E_{FexOy} - N_{Au}E_{Au\ atom\ in\ bulk}}{N_{Au\ on\ surface}} \quad \ldots \text{Equation 2.}$$

where E_i is the DFT calculated ground state energy of system i and N_{Au} is number of Au atoms and a more negative value of the binding energy indicates stronger binding.

The total energy of bulk Au is corrected for nanoparticle size effects using the Gibbs – Thompson relation. The binding energy of Au (111) on the Fe terminated surface (O terminated surface) is represented as blue bars (orange bars) in Figure 2.24a. Au (111) interacts very weakly with the O terminated surface as evidenced by the positive binding energies. In contrast, the adsorption energy of Au (111) on iron terminated surfaces is quite exothermic, being -0.37 eV for Fe_2O_3 (0001), -0.28 eV for Fe_3O_4 (111), -0.86 eV for FeO (111) and finally -0.72 eV for Fe (110). Moreover, the monotonic decrease in the binding energy of Au (111) with progressively lower oxidation state of iron shows increased interaction between Au and the iron oxide surface upon reduction.

Such a trend qualitatively confirms the electron microscopy and XPS observations which report a flattening of Au nanoparticles concomitant with reduction of the Au/iron oxide interface with increasing temperature. These DFT calculations were combined with thermodynamic relations to construct *ab initio* phase diagrams of Au films supported on Fe_3O_4 (111) as well as Fe_2O_3 (0001). The phase diagrams show that at low oxygen chemical potentials (representing high temperatures and low oxygen partial pressures), Au (111) films on reduced iron oxide are the thermodynamically most stable phase, while at higher oxygen chemical potentials, the iron oxide supports without any Au films shows highest stability.

This is line with experimental observations that flattening of Au nanoparticles occurs at higher temperatures. Finally, our calculations show that the oxygen vacancy formation energy for FeO (111) is lowered by 0.74 eV in the presence of an Au film, indicating that formation of oxygen vacancy in FeO becomes significantly more favorable in presence of

Au. Such trends are observed on FeO (100) too, where vacancy formation energy decreases by 0.96 eV in the presence of Au. This evidence, concomitant with XPS results demonstrate that Au NPs accelerate the latter stages of reduction of iron oxide.

Overall, DFT calculations show progressively stronger binding of thin Au films with reduction of iron oxide support, in line with experimental observations. The phase diagrams further confirm stability of Au films under UHV with increasing temperature. Thus, stronger adhesion of thin films on reduced iron oxide and more favorable oxygen vacancy formation in the presence of Au, cause increased stability of Au thin films on reduced iron oxide surfaces at high temperatures. This qualitatively confirms the SMSB between Au and Fe_3O_4 DNPs as evidenced by the flattening of Au films through the *in-situ* TEM experiment.

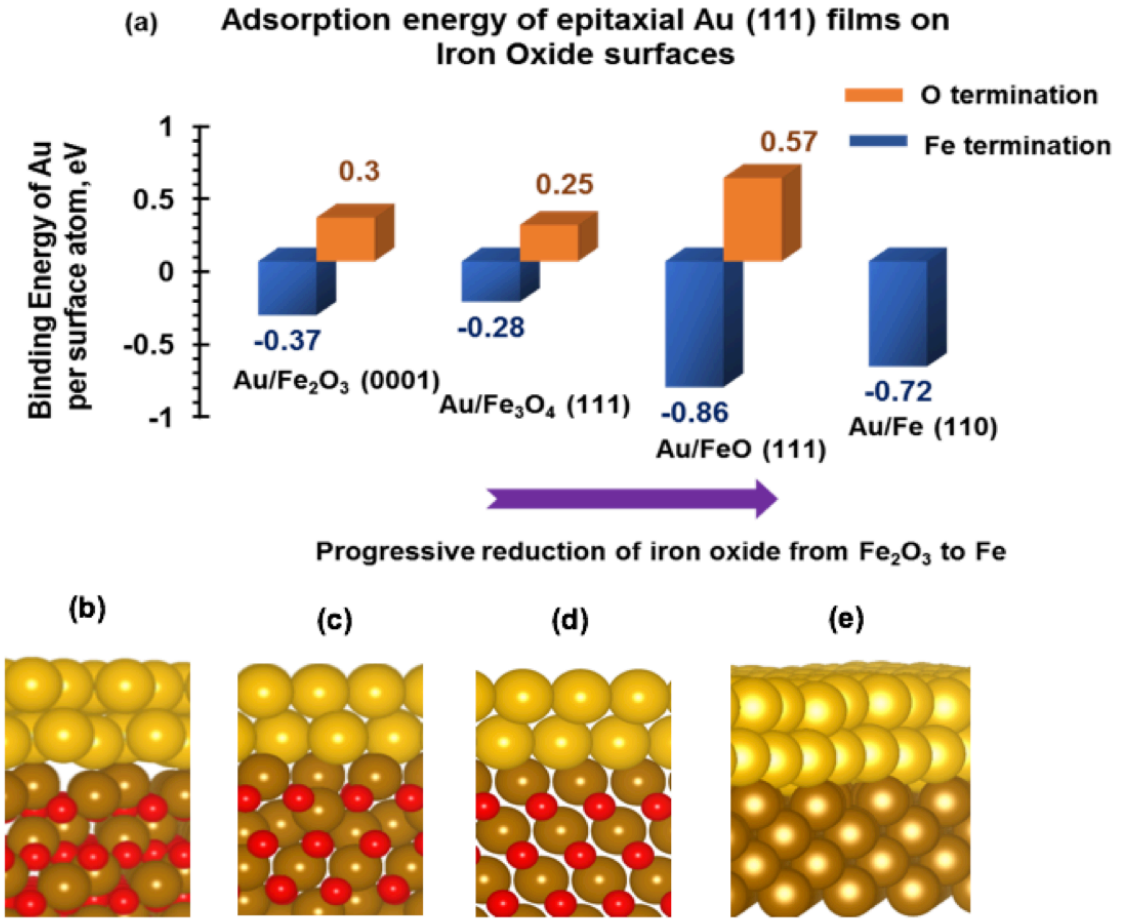

Figure 2.24 Trends in binding energies of epitaxial Au (111) films as iron oxide is progressively reduced from Fe_2O_3 to Fe. Binding on the Fe terminated surfaces (blue) is significantly more favorable in comparison with O terminated surfaces (orange). The monotonic reduction in binding energy confirms stronger adsorption of Au as the iron oxide is reduced, corroborating surface science studies. (b) 2 ML Au film supported on the 2-Fe termination of Fe_2O_3 (0001). (c) 2 ML Au film supported on the oct-1 Fe_3O_4 (111) termination. (d) 2 ML Au film adsorbed on Fe terminated FeO (111) surface. (e) 2 ML Au (111) film adsorbed on metallic Fe (110) surface. Au atoms are in yellow, Fe atoms in brown and O atoms are shown in red. (Data was collected and provided by Tej Choski, Paulami Majumdar, and Prof. Jeffrey Greeley)

2.4.4 Conclusions

In summary, we have shown that gold NPs of the DNPs were flattened and completely covered the iron oxide domain of the DNPs using *in-situ* TEM. This drastic morphological change of Au representing a FvdM mode is a direct evidence of the SMSB between gold and iron oxide, which was occurred during the vacuum annealing. The origin of the SMSB observed from the DNPs is attributed to the higher reducibility and higher concentration of the surface oxygen vacancies of the spherical nanoFe_3O_4 (i.e., iron oxide domains of the DNPs): *in-situ* STEM-EELS showed that the Au covered part of the nanoFe_3O_4 was highly reduced. XPS experiments showed that the nanoFe_3O_4 NPs were readily reduced during the vacuum annealing, while Fe_3O_4 thin film was highly stable against surface reduction. A series of our experimental results suggests a strong correlation between the wetting/SMSB and the surface reduction. DFT calculations also revealed that thin Au films will have a stronger bonding as the iron oxide support is further reduced.

The SMSB observed in the Au-Fe_3O_4 DNPs is not only physically interesting but also is practically important, because it emphasize the importance of the size and morphology control of a metal oxide support for tuning the metal-support bonding and it opens a possibility of preparing highly stable Au catalysts by optimizing the support size. In this regard, it is worth to revisit pre-existing metal oxide supports and carefully investigate their size dependent properties, because the metal-support interaction might be totally different with respect to the morphology and the size of materials, as we observed. More importantly, this work demonstrates the importance of nano-engineering

to develop novel materials from pre-existing materials ultimately for the development of improved catalysts and highly stable functional nanostructures for other applications, such as energy storage and conversion devices.

CHAPTER 3. CONCLUSIONS

Advanced TEM techniques including electron tomography, sequential aberration-corrected STEM imaging, and *in-situ* TEM have been developed and/or been used to characterize various heterogeneous catalysts. Within the philosophy of the Multidimensional Electron Microscopy, many length scales (from atomic to meso scale) and dynamics of the heterogeneous catalysts have been investigated at the same time by combining advanced TEM techniques. Especially, chapter 2.4 demonstrates how multidimensional approach (time + space + energy loss) in TEM can solve a scientific nature of the unusual thermal behaviors of Au-Fe_3O_4 dumbbell-like nanoparticles.

LIST OF REFERENCES

LIST OF REFERENCES

1. Chorkendorff, I. & Niemantsverdriet, J. W. *Concepts of Modern Catalysis and Kinetics*. (Wiley-VCH, 2006).

2. Williams, W. D. *et al.* Metallic corner atoms in gold clusters supported on rutile are the dominant active site during water-gas shift catalysis. *J. Am. Chem. Soc.* **132,** 14018–14020 (2010).

3. Midgley, P. A. & Thomas, J. M. Multi-dimensional electron microscopy. *Angew. Chemie - Int. Ed.* **53,** 8614–8617 (2014).

4. Argyle, M. & Bartholomew, C. Heterogeneous Catalyst Deactivation and Regeneration: A Review. *Catalysts* **5,** 145–269 (2015).

5. Han, C. W. & Ortalan, V. Secondary signal imaging (SSI) electron tomography (SSI-ET): A new three-dimensional metrology for mesoscale specimens in transmission electron microscope. *Micron* **76,** 62–67 (2015).

6. Han, C. W. *et al.* Highly Stable Bimetallic AuIr/TiO_2 Catalyst: Physical Origins of the Intrinsic High Stability against Sintering. *Nano Lett.* **15,** 8141–8147 (2015).

7. Han, C. W. *et al.* Migration of Single Iridium Atoms and Tri-iridium Clusters on MgO Surfaces: Aberration-Corrected STEM Imaging and Ab Initio Calculations. *J. Phys. Chem. Lett.* **6,** 4675–4679 (2015).

8. Midgley, P. A., Weyland, M., Thomas, J. M. & Johnson, B. F. G. Z-Contrast tomography: a technique in three-dimensional nanostructural analysis based on Rutherford scattering. *Chem. Commun.* 907–908 (2001).

9. Weyland, M., Midgley, P. A. & Thomas, J. M. Electron Tomography of Nanoparticle Catalysts on Porous Substrates: A New Technique Based on Rutherford Scattering. *J. Phys. Chem. B* **105,** 7882–7886 (2001).

10. Arslan, I., Yates, T. J. V., Browning, N. D. & Midgley, P. A. Embedded Nanostructures Revealed in Three Dimensions. *Science* **309,** 2195–2198 (2005).

11. Midgley, P. A. & Weyland, M. 3D electron microscopy in the physical sciences: The development of Z-contrast and EFTEM tomography. *Ultramicroscopy* **96,** 413–431 (2003).

12. Ercius, P., Weyland, M., Muller, D. A. & Gignac, L. M. Three-dimensional imaging of nanovoids in copper interconnects using incoherent bright field tomography. *Appl. Phys. Lett.* **88,** 1–4 (2006).

13. Van den Broek, W. *et al.* Correction of non-linear thickness effects in HAADF STEM electron tomography. *Ultramicroscopy* **116,** 8–12 (2012).

14. Hawkes, P. W. in *Electron Tomography* (ed. Frank, J.) 83–111 (Springer, 2006).

15. Loos, J. *et al.* Electron tomography on micrometer-thick specimens with nanometer resolution. *Nano Lett.* **9,** 1704–1708 (2009).

16. Sourty, E. *et al.* Tomographic imaging ultra-thick specimens with nanometer resolution. in *The European Microscopy Congress* **1,** 335–336 (2008).

17. Ortalan, V., Li, Y., Lavernia, E. J. & Browning, N. D. Electron Tomography of ZnO Nanocones with Secondary Signals in TEM. in *The European Microscopy Congress* **1,** 331–332 (2008).

18. Fakron, O. M. & Field, D. P. 3D image reconstruction of fiber systems using electron tomography. *Ultramicroscopy* **149,** 21–25 (2014).

19. Venkatakrishnan, S. V *et al.* A model based iterative reconstruction algorithm for high angle annular dark field-scanning transmission electron microscope (HAADF-STEM) tomography. *IEEE Trans. Image Process.* **22,** 4532–4544 (2013).

20. Demers, H. *et al.* Three-dimensional electron microscopy simulation with the CASINO Monte Carlo software. *Scanning* **33,** 135–146 (2011).

21. Salvat, F., Jablonski, A. & Powell, C. J. Elsepa - Dirac partial-wave calculation of elastic scattering of electrons and positrons by atoms, positive ions and molecules. *Comput. Phys. Commun.* **165,** 157–190 (2005).

22. Reichelt, R. in *Science of Microscopy* (eds. Hawkes, P. W. & Spence, J. C. H.) 170 (Springer, 2007).

23. Inada, H. *et al.* Atomic imaging using secondary electrons in a scanning transmission electron microscope: Experimental observations and possible mechanisms. *Ultramicroscopy* **111,** 865–876 (2011).

24. Zhu, Y., Inada, H., Nakamura, K. & Wall, J. Imaging single atoms using secondary electrons with an aberration-corrected electron microscope. *Nat. Mater.* **8,** 808–812 (2009).

25. Kremer, J. R., Mastronarde, D. N. & McIntosh, J. R. Computer visualization of three-dimensional image data using IMOD. *J. Struct. Biol.* **116,** 71–76 (1996).

26. Cnudde, V. & Boone, M. N. High-resolution X-ray computed tomography in geosciences: A review of the current technology and applications. *Earth-Science Rev.* **123,** 1–17 (2013).

27. Ortalan, V., Herrera, M., Morgan, D. G. & Browning, N. D. Application of image processing to STEM tomography of low-contrast materials. *Ultramicroscopy* **110,** 67–81 (2009).

28. Hutchings, G. J. Vapor Phase Hydrochlorination of Acetylene: Correlation of Catalytic Activity of Supported Metal Chloride Catalysts. *J. Catal.* **96,** 292–295 (1985).

29. Haruta, M., Kobayashi, T., Sano, H. & Yamada, N. Novel Gold Catalysts for the Oxidation of Carbon Monoxide at a Temperature far Below 0 Degree C. *Chem. Lett.* 405–408 (1987).

30. Hutchings, G. J. New Directions in Gold Catalysis. *Gold Bull.* **37,** 3–11 (2004).

31. Enache, D. I. *et al.* Solvent-Free Oxidation of Primary Alcohols to Aldehydes Using Au-Pd/TiO_2 Catalysts. *Science* **311,** 362–365 (2006).

32. Hughes, M. D. *et al.* Tunable gold catalysts for selective hydrocarbon oxidation under mild conditions. *Nature* **437,** 1132–1135 (2005).

33. Ishida, T. & Haruta, M. Gold Catalysts: Towards Sustainable Chemistry. *Angew. Chemie - Int. Ed.* **46,** 7154–7156 (2007).

34. Gates, B. C. Supported gold catalysts: new properties offered by nanometer and sub-nanometer structures. *Chem. Commun.* **49,** 7876–7877 (2013).

35. Choudhary, T. V. & Goodman, D. W. Oxidation catalysis by supported gold nano-clusters. *Top. Catal.* **21,** 25–34 (2002).

36. Jose-Yacaman, M. *et al.* Surface Diffusion and Coalescence of Mobile Metal Nanoparticles. *J. Phys. Chem. B* **109,** 9703–9711 (2005).

37. Bokhimi, X., Zanella, R. & Angeles-Chavez, C. Rutile-Supported Ir, Au, and Ir-Au Catalysts for CO Oxidation. *J. Phys. Chem. C* **114,** 14101–14109 (2010).

38. Kirchhoff, M., Specht, U. & Veser, G. Engineering high-temperature stable nanocomposite materials. *Nanotechnology* **16,** S401–S408 (2005).

39. Joo, S. H. *et al.* Thermally stable Pt/mesoporous silica core-shell nanocatalysts for high-temperature reactions. *Nat. Mater.* **8,** 126–131 (2009).

40. Biener, M. M. *et al.* ALD functionalized nanoporous gold: Thermal stability, mechanical properties, and catalytic activity. *Nano Lett.* **11,** 3085–3090 (2011).

41. Lu, J. *et al.* Coking- and Sintering-Resistant Palladium Catalysts Achieved Through Atomic Layer Deposition. *Science* **335,** 1205–1208 (2012).

42. Dai, Y. *et al.* A sinter-resistant catalytic system based on platinum nanoparticles supported on TiO_2 nanofibers and covered by porous silica. *Angew. Chemie - Int. Ed.* **49,** 8165–8168 (2010).

43. Yeung, C. M. Y. *et al.* Engineering Pt in ceria for a maximum metal-support interaction in catalysis. *J. Am. Chem. Soc.* **127,** 18010–18011 (2005).

44. Park, J. N. *et al.* Highly active and sinter-resistant Pd-nanoparticle catalysts encapsulated in silica. *Small* **4,** 1694–1697 (2008).

45. Prieto, G., Zečević, J., Friedrich, H., de Jong, K. P. & de Jongh, P. E. Towards stable catalysts by controlling collective properties of supported metal nanoparticles. *Nat. Mater.* **12,** 34–39 (2013).

46. Zhang, H., Watanabe, T., Okumura, M., Haruta, M. & Toshima, N. Catalytically highly active top gold atom on palladium nanocluster. *Nat. Mater.* **11,** 49–52 (2012).

47. Shiraishi, Y., Sakamoto, H., Sugano, Y., Ichikawa, S. & Hirai, T. Pt-Cu Bimetallic Alloy Nanoparticles Supported on Anatase TiO_2 : Highly Active Catalysts for Aerobic Oxidation Driven by Visible Light. *ACS Nano* **7,** 9287–9297 (2013).

48. Cao, A. & Veser, G. Exceptional high-temperature stability through distillation-like self-stabilization in bimetallic nanoparticles. *Nat. Mater.* **9,** 75–81 (2010).

49. Gómez-Cortés, A. *et al.* Au-Ir/TiO_2 prepared by Deposition Precipitation with Urea: Improved Activity and Stability in CO oxidation. *J. Phys. Chem. C* **113,** 9710–9720 (2009).

50. Guan, Y. & Hensen, E. J. M. Selective oxidation of ethanol to acetaldehyde by Au-Ir catalysts. *J. Catal.* **305,** 135–145 (2013).

51. Liu, X., Wang, A., Wang, X., Mou, C.-Y. & Zhang, T. Au-Cu Alloy nanoparticles confined in SBA-15 as a highly efficient catalyst for CO oxidation. *Chem. Commun.* 3187–3189 (2008).

52. Liu, X. *et al.* Synthesis of thermally stable and highly active bimetallic Au-Ag nanoparticles on inert supports. *Chem. Mater.* **21,** 410–418 (2009).

53. Sandoval, A., Louis, C. & Zanella, R. Improved activity and stability in CO oxidation of bimetallic Au-Cu/TiO_2 catalysts prepared by deposition-precipitation with urea. *Appl. Catal. B Environ.* **140–141,** 363–377 (2013).

54. Batson, P. E., Dellby, N. & Krivanek, O. L. Sub-ångstrom resolution using aberration corrected electron optics. *Nature* **418,** 617–620 (2002).

55. Krivanek, O. L. *et al.* Atom-by-atom structural and chemical analysis by annular dark-field electron microscopy. *Nature* **464,** 571–574 (2010).

56. Arslan, I., Walmsley, J. C., Rytter, E., Bergene, E. & Midgley, P. A. Toward three-dimensional nanoengineering of heterogeneous catalysts. *J. Am. Chem. Soc.* **130,** 5716–5719 (2008).

57. Thomas, J. M. *et al.* The chemical application of high-resolution electron tomography: Bright field or dark field? *Angew. Chemie* **116,** 6913–6915 (2004).

58. Ward, E. P. W., Yates, T. J. V, Fernández, J. J., Vaughan, D. E. W. & Midgley, P. A. Three-dimensional nanoparticle distribution and local curvature of heterogeneous catalysts revealed by electron tomography. *J. Phys. Chem. C* **111,** 11501–11505 (2007).

59. González, J. C. *et al.* 3 D Characterization of Gold Nanoparticles Supported on Heavy Metal Oxide Catalysts by HAADF-STEM Electron Tomography. *Angew. Chemie* **121,** 5417–5419 (2009).

60. Kresse, G. & Furthmüller, J. Efficient iterative schemes for ab initio total-energy calculations using a plane-wave basis set. *Phys. Rev. B* **54,** 11169–11186 (1996).

61. Kresse, G. & Joubert, D. From ultrasoft pseudopotentials to the projector augmented-wave method. *Phys. Rev. B* **59,** 1758–1775 (1999).

62. Perdew, J. P. *Electronic Structure of Solids*. (Akademie Verlag, 1999).

63. Diebold, U., Ruzycki, N., Herman, G. S. & Selloni, A. One step towards bridging the materials gap: Surface studies of TiO2 anatase. *Catal. Today* **85,** 93–100 (2003).

64. Liu, J. J. Advanced Electron Microscopy of Metal-Support Interactions in Supported Metal Catalysts. *ChemCatChem* **3,** 934–948 (2011).

65. Tewari, A. & Gokhale, A. M. Nearest-neighbor distances between particles of finite size in three-dimensional uniform random microstructures. *Mater. Sci. Eng. A* **385,** 332–341 (2004).

66. Hernandez-Garrido, J. C. *et al.* The location of gold nanoparticles on titania: A study by high resolution aberration-corrected electron microscopy and 3D electron tomography. *Catal. Today* **160,** 165–169 (2011).

67. Kittel, C. *Introduction to Solid State Physics*. (Wiley, 1986).

68. Mavrikakis, M., Stoltze, P. & Nørskov, J. K. Making gold less noble. *Catal. Letters* **64,** 101–106 (2000).

69. Li, L. *et al.* Investigation of Catalytic Finite-Size-Effects of Platinum Metal Clusters. *J. Phys. Chem. Lett.* **4,** 222–226 (2013).

70. Farmer, J. A. & Campbell, C. T. Ceria Maintains Smaller Metal Catalyst Particles by Strong Metal-Support Bonding. *Science* **329,** 933–936 (2010).

71. Bartholomew, C. H. Mechanism of catalyst deactivation. *Appl. Catal. A Gen.* **212,** 17–60 (2001).

72. Sloan, P. A. Time-resolved scanning tunnelling microscopy for molecular science. *J. Phys. Condens. matter* **22,** 264001 (2010).

73. Li, S.-C., Chu, L.-N., Gong, X.-Q. & Diebold, U. Hydrogen Bonding Controls the Dynamics of Catechol Adsorbed on a TiO_2(110) Surface. *Science* **328,** 882–884 (2010).

74. Parkinson, G. S. *et al.* Carbon monoxide-induced adatom sintering in a Pd-Fe3O4 model catalyst. *Nat. Mater.* **12,** 724–728 (2013).

75. Bliem, R. *et al.* Cluster nucleation and growth from a highly supersaturated adatom phase: Silver on magnetite. *ACS Nano* **8,** 7531–7537 (2014).

76. Ishikawa, R. *et al.* Direct observation of dopant atom diffusion in a bulk semiconductor crystal enhanced by a large size mismatch. *Phys. Rev. Lett.* **113,** 155501 (2014).

77. Woehl, T. J., Evans, J. E., Arslan, I., Ristenpart, W. D. & Browning, N. D. Direct in situ determination of the mechanisms controlling nanoparticle nucleation and growth. *ACS Nano* **6,** 8599–8610 (2012).

78. Abellan, P. *et al.* Probing the Degradation Mechanisms in Electrolyte Solutions for Li-Ion Batteries by in Situ Transmission Electron Microscopy. *Nano Lett.* **14,** 1293–1299 (2014).

79. Evans, J. E. *et al.* Visualizing macromolecular complexes with in situ liquid scanning transmission electron microscopy. *Micron* **43,** 1085–1090 (2012).

80. Hansen, P. L. *et al.* Atom-resolved imaging of dynamic shape changes in supported copper nanocrystals. *Science* **295,** 2053–2055 (2002).

81. Yoshida, H. *et al.* Visualizing Gas Molecules Interacting with Supported Nanoparticulate Catalysts at Reaction Conditions. *Science* **335,** 317–319 (2012).

82. Yuk, J. M. *et al.* High-Resolution EM of Colloidal Nanocrystal Growth Using Graphene Liquid Cells. *Science* **336,** 61–64 (2012).

83. Liao, H. G. *et al.* Facet development during platinum nanocube growth. *Science* **345,** 916–919 (2014).

84. Pennycook, S. J. *et al.* Aberration-corrected scanning transmission electron microscopy: from atomic imaging and analysis to solving energy problems. *Philos. Trans. R. Soc. A* **367,** 3709–3373 (2009).

85. Ortalan, V., Uzun, A., Gates, B. C. & Browning, N. D. Towards full-structure determination of bimetallic nanoparticles with an aberration-corrected electron microscope. *Nat. Nanotechnol.* **5,** 843–847 (2010).

86. Batson, P. E. Motion of gold atoms on carbon in the aberration-corrected STEM. *Microsc. Microanal.* **14,** 89–97 (2008).

87. Batson, P. E. *et al.* Plasmonic nanobilliards: Controlling nanoparticle movement using forces induced by swift electrons. *Nano Lett.* **11,** 3388–3393 (2011).

88. Lu, J., Aydin, C., Browning, N. D., Wang, L. & Gates, B. C. Sinter-resistant catalysts: Supported iridium nanoclusters with intrinsically limited sizes. *Catal. Letters* **142,** 1445–1451 (2012).

89. Uzun, A., Ortalan, V., Browning, N. D. & Gates, B. C. Site-isolated iridium complexes on MgO powder: individual Ir atoms imaged by scanning transmission electron microscopy. *Chem. Commun.* **7345,** 4657–4659 (2009).

90. Wnuk, J. D. *et al.* Electron Induced Surface Reactions of the Organometallic Precursor Trimethyl (methylcyclopentadienyl) platinum (IV) Electron Induced Surface Reactions of the Organometallic Precursor Trimethyl (methylcyclopentadienyl) platinum (IV). *J. Phys. Chem. C* **113,** 2487–2496 (2009).

91. Wnuk, J. D. *et al.* Electron beam deposition for nanofabrication: Insights from surface science. *Surf. Sci.* **605,** 257–266 (2011).

92. Jenke, M. G. *et al.* Toward local growth of individual nanowires on three-dimensional microstructures by using a minimally invasive catalyst templating method. *Nano Lett.* **11,** 4213–4217 (2011).

93. Riazanova, A. V, Rikers, Y. G. M., Mulders, J. J. L. & Belova, L. M. Pattern shape control for heat treatment purification of electron-beam-induced deposition of gold from the Me2Au(acac) precursor. *Langmuir* **28,** 6185–6191 (2012).

94. Botman, A., Mulders, J. J. L., Weemaes, R. & Mentink, S. Purification of platinum and gold structures after electron-beam-induced deposition. *Nanotechnology* **17,** 3779–3785 (2006).

95. Van Kouwen, L., Botman, A. & Hagen, C. W. Focused electron-Beam-induced deposition of 3 nm dots in a scanning electron microscope. *Nano Lett.* **9,** 2149–2152 (2009).

96. Kresse, G. & Furthmuller, J. Efficiency of ab-initio total energy calculations for metals and semiconductors using a plane-wave basis set. *Comput. Mater. Sci.* **6,** 15–50 (1996).

97. Perdew, J. P. & Wang, Y. Accurate and simple analytic representation of the electron-gas correlation energy. *Phys. Rev. B* **45,** 13244–13249 (2015).

98. Blöchl, P. E. Projector augmented-wave method. *Phys. Rev. B* **50,** 17953–17979 (1994).

99. Monkhorst, H. J. & Pack, J. D. Special points for Brillouin-zone integrations. *Phys. Rev. B* **13,** 5188–5192 (1977).

100. Lu, J., Serna, P. & Gates, B. C. Zeolite- and MgO-supported molecular iridium complexes: Support and ligand effects in catalysis of ethene hydrogenation and H-D exchange in the conversion of H2 + D2. *ACS Catal.* **1,** 1549–1561 (2011).

101. Zhukovskii, Y. F., Kotomin, E. A., Jacobs, P. W. M., Stoneham, A. M. & Harding, J. H. Comparative theoretical study of the Ag-MgO (100) and (110) interfaces. *Surf. Sci.* **441,** 373–383 (1999).

102. Dąbrowski, J. & Scheffler, M. Self-consistent study of the electronic and structural properties of the clean Si(001)(2×1) surface. *Appl. Surf. Sci.* **56–58,** 15–19 (1992).

103. Mills, G., Jonsson, H. & Schenter, G. K. Reversible work transition state theory: application to dissociative adsorption of hydrogen. *Surf. Sci.* **324,** 305–337 (1995).

104. Farmer, J. A. & Campbell, C. T. Catalyst Particles by Strong Metal-Support Bonding. *Science* **329,** 933–936 (2010).

105. Hashmi, A. S. K. & Hutchings, G. J. Gold Catalysis. *Angew. Chemie - Int. Ed.* **45,** 7896–7936 (2006).

106. Fu, Q., Weber, A. & Flytzani-Stephanopoulos, M. Nanostructured Au-CeO2 catalysts for low-temperature water-gas shift. *Catal. Letters* **77,** 87–95 (2001).

107. Fu, Q., Saltsburg, H. & Flytzani-stephanopoulos, M. Active Nonmetallic Au and Pt Species on Ceria-Based Water-Gas Shift Catalysts. *Science* **301,** 935–938 (2003).

108. Rodriguez, J. A. *et al.* Activity of CeOx and TiO_x Nanoparticles Grown on Au(111) in the Water-Gas Shift Reaction. *Science* **318,** 1757–1760 (2007).

109. Ta, N. *et al.* Stabilized Gold Nanoparticles on Ceria Nanorods by Strong Interfacial Anchoring. *J. Am. Chem. Soc.* **134,** 20585–20588 (2012).

110. Boucher, M. B., Goergen, S., Yi, N. & Flytzani-Stephanopoulos, M. 'Shape effects' in metal oxide supported nanoscale gold catalysts. *Phys. Chem. Chem. Phys.* **13,** 2517–2527 (2011).

111. Carrettin, S., Concepción, P., Corma, A., López Nieto, J. M. & Puntes, V. F. Nanocrystalline CeO_2 increases the activity of Au for CO oxidation by two orders of magnitude. *Angew. Chemie - Int. Ed.* **43,** 2538–2540 (2004).

112. Peng, S. *et al.* A Facile Synthesis of Monodisperse Au Nanoparticles and Their Catalysis of CO Oxidation. *Nano Res* **1,** 229–234 (2008).

113. Yu, H., Chen, M., Rice, P. M., Wang, S. X. & White, R. L. Dumbbell-like Bifunctional Au−Fe_3O_4 Nanoparticles. *Nano Lett.* **5,** 379–382 (2005).

114. Yin, H. *et al.* Colloidal deposition synthesis of supported gold nanocatalysts based on Au-Fe_3O_4 dumbbell nanoparticles. *Chem. Commun.* 4357–4359 (2008).

115. Lee, Y., Garcia, M. A., Frey Huls, N. A. & Sun, S. Synthetic tuning of the catalytic properties of Au-Fe3O 4 nanoparticles. *Angew. Chemie - Int. Ed.* **49,** 1271–1274 (2010).

116. Thevenaz, P., Ruttimann, U. E. & Unser, M. A pyramid approach to subpixel registration based on intensity. *IEEE Trans. Image Process.* **7,** 27–41 (1998).

117. Schneider, C. a, Rasband, W. S. & Eliceiri, K. W. NIH Image to ImageJ: 25 years of image analysis. *Nat. Methods* **9,** 671–675 (2012).

118. Hanwell, M. D., Ayachit, U., Muller, D. A. & Hovden, R. Tomviz.org.

119. Gatel, C. & Snoeck, E. Comparative study of Pt, Au and Ag growth on Fe_3O_4(001) surface. *Surf. Sci.* **600,** 2650–2662 (2006).

120. Gatel, C. & Snoeck, E. Epitaxial growth of Au and Pt on Fe_3O_4(111) surface. *Surf. Sci.* **601,** 1031–1039 (2007).

121. Shaikhutdinov, S. K., Meyer, R., Naschitzki, M., Bäumer, M. & Freund, H. J. Size and support effects for CO adsorption on gold model catalysts. *Catal. Letters* **86,** 211–219 (2003).

122. Santos-Carballal, D., Roldan, A., Grau-Crespo, R. & de Leeuw, N. H. A DFT study of the structures, stabilities and redox behaviour of the major surfaces of magnetite Fe_3O_4. *Phys. Chem. Chem. Phys.* **16,** 21082–21097 (2014).

123. Zhao, L. *et al.* Morphology-controlled synthesis of magnetites with nanoporous structures and excellent magnetic properties. *Chem. Mater.* **20,** 198–204 (2008).

124. Wahlström, E. *et al.* Bonding of gold nanoclusters to oxygen vacancies on rutile TiO_2(110). *Phys. Rev. Lett.* **90,** 26101 (2003).

125. Chen, M. S. & Goodman, D. W. Interaction of Au with titania: The role of reduced Ti. *Top. Catal.* **44,** 41–47 (2007).

126. Lee, Y. *et al.* Raman Analysis of Mode Softening in Nanoparticle $CeO_{(2-\delta)}$ and Au-$CeO_{(2-\delta)}$ during CO Oxidation. *J. Am. Chem. Soc.* **133,** 12952–12955 (2011).

127. McIntyre, N. S. & Zetaruk, D. G. X-ray photoelectron spectroscopic studies of iron oxides. *Anal. Chem.* **49,** 1521–1529 (1977).

128. Grosvenor, A. P., Kobe, B. A., Biesinger, M. C. & McIntyre, N. S. Investigation of multiplet splitting of Fe 2p XPS spectra and bonding in iron compounds. *Surf. Interface Anal.* **36,** 1564–1574 (2004).

129. Syed, S., Endo, Y., Sato, T., Kawamura, Y. & Nakatani, R. Change of Magnetic Properties and Structure in Fe_3O_4 Films on Si Substrates with Annealing Temperature. *Mater. Trans.* **49,** 175–178 (2008).

VITA

VITA

Chang Wan Han started his materials science studies at Korea University, Seoul, South Korea in 2002. When he was a sophomore student in the department of materials science and engineering, he met Prof. Sang Ho Lim and joined his research group as an undergraduate research assistant in December 2014. After two years of undergraduate research on the "CoFe based soft ferromagnetic thin film and its application on a high frequency noise suppressor," Chang Wan started his master study on magnetic random access memory and its exchange-coupled free layer in the same research group at Korea University. In February of 2012, Chang Wan joined the Central Advanced Research and Engineering Laboratory of Hyundai Motor Company, Gyeonngi-do, South Korea as a research engineer and he was responsible for developing fabrication processes for silicon carbide power Schottky barrier diode and trench gate MOSFTET until he left the company in June 2016. In July of 2012, Chang Wan moved to West Lafayette, Indiana and started his PhD work in the School of Materials Engineering at Purdue University.

He joined a new assistant professor Volkan Ortalan's group as the first student. During his PhD, he performed advanced transmission electron microscopy experiments to investigate atomic structures and dynamics of catalyst nanoparticles as a team member of the NSF DMREF project. Chang Wan completed his PhD in December 2016 with his thesis titled "Characterization of Heterogeneous Catalysts using Advanced Transmission Electron Microscopy Techniques."

PUBLICATIONS

PUBLICATIONS

1. A. Aguilar-Tapia, L. Delannoy, C. Louis, C. W. Han, V. Ortalan, and R. Zanella, "*Selective Hydrogenation of 1,3-butadiene over Bimetallic Au-Ni/TiO_2 Catalysts Prepared by Deposition-Precipitation with Urea*", *Journal of Catalysis* (in press, Oct. 2016)

2. M. A. Rubio, E. I. Gunduz, L. J. Groven, T. R. Sippel, C. W. Han, R. R. Unocic, V. Ortalan, and S. F. Son. "*Microexplosions and Ignition Dynamics in Engineered Aluminum/Polymer Fuel Particles*", *Combustion and Flame* (in press, Jul. 2016)

3. C. W. Han, P. Majumdar, E. E. Marinero, A. Aguilar-Tapia, R. Zanella, J. Greeley, and V. Ortalan, "*Highly Stable Bimetallic AuIr/TiO_2 Catalyst: Physical Origins of the Intrinsic High Stability against Sintering*", *Nano Letters*, 15, 8141-8147 (2015)

4. C. W. Han, H. Iddir, A. Uzun, L. A. Curtiss, N. D. Browning, B. C. Gates, and V. Ortalan, "*Migration of Single Iridium Atoms and Tri-iridium Clusters on MgO Surfaces: Aberration-Corrected STEM Imaging and Ab Initio Calculations*", *The Journal of Physical Chemistry Letters*, 16, 4675-4679 (2015)

5. C. W. Han and V. Ortalan, "*Secondary signal imaging (SSI) electron tomography (SSI-ET): A new three-dimensional metrology for mesoscale specimens in transmission electron microscope*", *Micron,* 76, 62-67 (2015)

6. C. W. Han, J. K. Han, and S. H. Lim, "*Thermal Stability of Nanostructured Synthetic Ferrimagnets under Applied Magnetic Fields in the 45^o direction*", *Journal of Magnetics*, 15, 116 (2010)

7. J. K. Han, C. W. Han, and S. H. Lim, "*Dependence of the Magnetic Energy Barrier on the Strength of Applied Magnetic Field in Nanostructured Cells of Exchange-Coupled Trilayers*", *Journal of Korean Physical Society*, 55, 2505 (2009)

8. C. W. Han and S. H. Lim, "*A Comparative Study on the Prediction of the Saddle Point Magnetic Configuration in Nanostructured Cells of Single Magnetic Thin Films and Synthetic Antiferromagnets*", *Japanese Journal of Applied Physics*, 48, 123001 (2009)

9. C. W. Han**,** J. K. Han, and S. H. Lim, "*Calculation of the Magnetic Energy Barrier in Nanostructured Cells of Synthetic Ferrimagnets*", *Journal of Applied Physics,* 106, 094508 (2009)
10. C. W. Han and S. H. Lim, "*Variation of the Magnetic Energy Barrier with the Cell Shape of Nanostructured Magnetic Thin Films*", *Journal of Physics D*, 42, 045006 (2009)

11. D. H. Lee, C. W. Han, and S. H. Lim, "*Calculation of Magnetostatic Fields in Nanostructured Ellipsoidal Cells of Exchange-Coupled Trilayers*", *Journal of Korean Physical Society*, 54, 169 (2009)